Mesoscale regulatory mechanisms of branch formation generating hierarchical structure of the lung

Running title: Lung models of branching scale control

Hisako Takigawa-Imamura,[1,*] Hiroaki Takesue,[2, 3] and Takashi Miura [1]

[1]Anatomy and Cell Biology, Graduate School of Medical Sciences, Kyushu University, 3-1-1 Maidashi, Higashi-ku, Fukuoka 812-8582, Japan

[2]Graduate School of Pharmaceutical Sciences, Kyushu University, 3-1-1 Maidashi, Higashi-ku, Fukuoka 812-8582, Japan

*Correspondence: imamura.hisako.024@m.kyushu-u.ac.jp

[3]Hiroaki Takesue's present address is Biochemistry, Graduate School of Medical Sciences, Kyushu University, 3-1-1 Maidashi, Higashi-ku, Fukuoka 812-8582, Japan.

Abstract

The lung airways are characterized by long and wide proximal branches and short and thin distal branches. In this study, we investigated the emergence of this hierarchical structure through experimental observations and computational models. We focused on the branch formation in the pseudoglandular stage and examined the response of mouse lung epithelium to fibroblast growth factor 10 (FGF10) by monitoring extracellular signal-regulated kinase (ERK) activity. The ERK activity increased depending on the epithelial tissue curvature. This curvature-dependent response decreased as the development progressed. Therefore, to understand how these epithelial changes affect branching morphology, we constructed a computational model of curvature-dependent epithelial growth. We demonstrated that branch length was controlled by the curvature dependence of growth that was consistent with the experimental observations and lung morphology. However, the branching of the thin branches is suppressed in this model, which is inconsistent with the fact that thin branches in the lung are short. Thus, we introduced branch formation by apical constriction, which was shown to be regulated by Wnt signaling in our previous studies. Mathematical analysis indicated that the effect of apical constriction is cell shape-dependent, suggesting that apical constriction ameliorates the branching of thin branches. Finally, we were able to provide clarity on the hierarchical branching structure through an integrated computational model of curvature-dependent growth and cell shape regulation. We proposed that curvature-dependent growth involving FGF and Wnt-mediated cell shape regulation coordinate to control the spatial scale and frequency of branch formation.

Statement of Significance

The lung airways exhibit a morphology in which the branch scale continuously decreases toward the distal side. This study explains the mechanism behind the hierarchical branching structure. Computational models proposed that the epithelial growth activity and apical constriction cooperatively determine branch length and tip width, consistent with the experimental observations that epithelial properties change as development progresses. The growth activity and cell shape are regulated by FGF and Wnt signaling, respectively, suggesting the importance of these pathways in patterning branch structures at a different scale. Our study provides a new perspective on the role of epithelial properties in the regulation of the mesoscale structure of the lung via FGF and Wnt signaling, thereby providing an understanding of branching morphogenesis.

Introduction

Mammalian lung airways exhibit an intricate tree-like structure that contributes to the efficiency of respiratory function. The lung airways are formed by repetitive elongation and bifurcation of the epithelial tube, which is common in organs such as blood vessels, kidneys, and glandular organs. The architecture of major airways (such as the main bronchi, lobar bronchi, and segmental bronchi) shows a stereotyped pattern in humans (1–3), suggesting the existence of a mechanism to program the large-scale design. In mouse lungs, early formed proximal branch segments are thick and long; in contrast, distal branch segments become thinner and shorter (4–6). Unlike the botanical tree, in

which new branches are always thin, the lumen size of the lung epithelial tip is large in the early stage and decreases as bifurcation proceeds. In addition, branching events occur more frequently as development progresses (4, 7–9), suggesting that branch formation is controlled with the developmental phase to configure the hierarchical structure. Several biological and theoretical investigations have explored the principle of epithelial branching through the epithelial-mesenchymal interactions (10–16), whereas little is known about how the macroscopic configuration is ordered. In this study, we aimed to address the regulation of changes in the branch diameter and segment length during lung development.

Epithelial-mesenchymal interaction is mediated by diffusible molecules such as fibroblast growth factor (FGF), bone morphogenic protein (BMP), sonic hedgehog (Shh), and Wnt (17, 18). Signaling molecules control the spatiotemporal coordination of cellular proliferation, migration, differentiation, and shape, leading to the arrangement of various cells in the prescribed shape for tissue formation. During lung development, epithelial growth is mainly promoted by FGF10, which is expressed in the outermost boundary of the mesenchyme (11, 19, 20). FGF10 also induces epithelial expression of Shh, which diffuses into the mesenchyme and adversely represses FGF10 expression (21, 22). Theoretical studies have shown that this feedback interaction leads to interfacial instability in the growing epithelium and promotes epithelial branching (23). This is similar to the mechanism by which bacterial colonies grow under nutrient-deprived conditions, where regions of high curvature are exposed to residual nutrients and elongate faster than regions of low curvature (24, 25). The tendency of the tip to grow faster is a

common mechanism for spontaneous branch formation, such as crystal growth and viscous fingering (26–28). Branching and bud formation with patterned proliferative activity at branch tips have also been observed for epithelial explants in extracellular matrix gels with an unbiased FGF distribution supposed (10). The mechanism of how heterogeneity of growth activity emerges is unknown; thus, the profile of FGF signaling activity in the lung epithelium requires confirmation to verify the common concept of branch formation models.

Wnt is also crucial for lung development (18). The Wnt/ β-catenin pathway mediates cell fate determination in the embryonic state. In the lung mesenchyme, Wnt2 and Wnt2b are expressed as master regulators of proximal and distal patterning, which are distinguished by the epithelial expression of Sox2 and Sox9, respectively (29, 30). Loss of Wnt2/2b expression results in lung hypoplasia in the absence of small distal branches (31, 32). Double mutation of transcription factors Tbx2 and Tbx3, which act downstream of Shh and upstream of Wnt, respectively, also severely reduces the number of distal tips by inhibiting mesenchymal proliferation (33). These findings indicate that Wnt may contribute to the generation of distal branches in the lungs. We previously reported that Wnt switches epithelial development from the branching phase (called the pseudoglandular stage) to the alveolus-shaping phase (canalicular stage), emphasising the importance of Wnt signaling in distal duct morphology (34). It was also revealed that activation of the Wnt/β-catenin pathway induces apical constriction of the lung epithelium and eventually scales down the bud size that emerges in mesenchyme-free epithelial cyst culture. Bud formation is an *in vitro* model of branch formation; therefore,

our results indicate that Wnt signaling assists FGF10 in branching events. These results are consistent with a previous report showing that deletion of the Wnt receptor Fzd2 causes branching defects and cystic lung *in vivo* (35). In this study, we considered how the interplay of growth control by FGF10 and cell shape regulation by Wnt can adjust the branch scale.

There are two distinct modes of lung branching: tip splitting and lateral branching (4). The former is the symmetrical bifurcation at the distal end of a growing branch, and the latter is the sprouting in the middle of a branch. Stepwise observation of mouse lung development revealed that lateral branching mainly occurs during the early phase in the pseudoglandular stage, suggesting that lateral branching mainly generates asymmetric major branches. In contrast, tip splitting sequentially occurs in different sizes and frequencies during branch elongation, suggesting that the regulation of tip splitting is crucial for the hierarchical structure of branches. Accordingly, we focused on tip splitting in the pseudoglandular stage.

This study aimed to explore how branch formation is regulated in the lung through experimental and theoretical examinations. Experimental verification of the protrusion-grows-faster concept in the lung epithelium provides new insights into the tip-splitting branching frequency change across developmental stages through FGF. We also observed the change in cell size across the stages to explain the difference in tube size. Mathematical models demonstrate how these observed properties contribute to the hierarchical structure of the airways. Furthermore, we propose that apical constriction can efficiently promote tip splitting of thin branches to regulate their length based on

observation of cell shape changes and mathematical analysis.

Materials and Methods

Animal

Transgenic mice expressing ERK FRET biosensors (36) were kindly provided by Michiyuki Matsuda (Kyoto University, Kyoto, Japan) through the JCRB Laboratory Animal Resource Bank of the National Institute of Biomedical Innovation. ERK FRET biosensors, EKAREV-nuclear export signals, are localized in the cytoplasm. ICR mice (Japan Charles River, Yokohama, Japan) were crossed with EKAREV mice, and the embryos were used for ERK activity measurement. ICR embryos were used for FGF10 uptake assay and immunostaining. All procedures involving animal experiments were reviewed and approved by the Ethics Committee of Animal Experiments, Kyushu University Graduate School of Medical Sciences (A25-182, A27-071, and A29-036).

Mesenchyme-free culture of embryonic lung epithelium in Matrigel

Embryonic mouse lungs (E12.5, E13.5, and E14.5) were dissected and washed with Hank's balanced salt solution (HBSS). Lung lobes were cut into pieces and soaked in dispase solution (1 U/mL in HBSS; Gibco) for 10 min at 37 °C. The tissues were washed twice in 10 mL of HBSS. Repetitive pipetting of tissues in HBSS broke up the mesenchyme and small epithelial explants remained. The supernatant containing mesenchymal cells was removed using a Cell Strainer with 40-µm pores (Falcon). The epithelial explants were picked using a micropipette under a stereomicroscope and placed

on the bottom of a 35-mm glass-bottomed dish (IWAKI, blanched explants) or on the μ-Slide Angiogenesis slide (ibidi, small explants for FGF10 dose-dependent assay). Matrigel (Corning, No. 356237) containing recombinant human FGF10 protein (PeproTech) was overlaid on explants and allowed to solidify for 15 min at 37°C, followed by the addition of the medium (2 mL for 35-mm dishes, and 50 μm for a well of the angiogenesis slide). The tissue culture medium was DMEM/Ham's F-12 (Nacalai Tesque) supplied with Penicillin-Streptomycin Mixed Solution (×10, Nacalai Tesque), L-glutamine (584 mg/mL), and bovine serum albumin (10%). Samples were incubated for 18 h before ERK activity measurement. The FGF10 concentration is indicated as the mass concentration in the volume of the gel and medium.

ERK activity measurement

We used a 405 nm laser for excitation and acquired the 475 nm and 530 nm emissions as CFP and YFP signals, respectively. The acquired confocal images were analysed using Fiji software (National Institute for Health). Local ERK activity was estimated as the ratio of the YFP signal to the CFP signal in a small region of interest (ROI) with a diameter defined based on epithelium thickness (Figure 1 and S1). The ROI was limited in the regions where the signal of the epithelial cross section was clearly acquired in the confocal image (123 ROIs for E12.5, 108 ROIs for E13.5, and 77 ROIs for E14.5, Figure S1). Mean command in Fiji was used to reduce the effect of spatial noise before quantifying fluorescence intensity, and signal ratios were corrected for background signal. Next, 2D tissue curvature was calculated from a series of ROI centers. Curvature was

calculated from the coordinates of three ROIs four apart along adjacent data points to capture the smooth tissue curvature. The 3D curvature was not successful because of tissue damage caused by prolonged image acquisition times. The correlation with linear regression between ERK activity averaged over five neighbouring points and tissue curvature was calculated by using *Mathematica* (Wolfram Research, Inc.).

The ERK activity of the cyst (Figure 2A and S2A) was calculated as the ratio between the total intensities of YFP and CFP in the epithelial cyst area, excluding the luminal area in the cross-section. The FGF10 dose dependency was estimated by linear regression analysis, and its significant difference by developmental stage was tested using two-way analysis of variance (ANOVA) in the statistical software R (R Core Team).

FGF10 incorporation assay

Recombinant FGF10 protein was labeled using an Alexa Fluor 488 Microscale Protein Labeling Kit (Invitrogen). To reduce the loss of physiological activity of FGF10, we optimised the labeling protocol and reduced the amount of Alexa Fluor used. The labeling reaction was conducted by mixing 100 μL of FGF10 solution (1 μg/mL in phosphate-buffered saline [PBS], pH 7.4), 5 μL of sodium bicarbonate (1 M), and 9.8 μL of Alexa488 solution (1:10 diluted) at 22°C. After 15-min reaction, the unreacted dye in the sample was removed using a Slide-A-Lyser Mini Dialysis Unit (Thermo Scientific) in PBS for 16 h at 4°C. The purified solution was collected and the protein concentration was measured using a NanoDrop spectrophotometer (Thermo Fisher). The FGF10-Alexa488 solution was stored in small aliquots at −20°C to avoid freeze-thaw cycles.

Incubation and storage were performed in the dark.

Epithelial explants were embedded in Matrigel containing FGF10-Alexa488 protein in a 35-mm dish, which was subsequently filled with the medium. The protein incorporation was allowed for 3 h in a stage-top chamber (Tokai Hit) to maintain a 5% CO_2 controlled atmosphere at 37°C followed by observation. The relative uptake activity was measured as the mean fluorescent intensity in the epithelial area of the cross-section of each explant. ROIs were defined as the round epithelial area, excluding the luminal area in the cross section. Although epithelial explants of E14.5 tended to form a cyst for 3 h, explants of E13.5 were slow to form a cyst, and most ROIs were obtained in sections of tip regions (Figure S2B).

FGF10 uptake was quantified as the mean intensity in the epithelial cyst area, excluding the luminal area in the cross-section. The FGF10 dose dependency was estimated by linear regression analysis, and its significant difference by developmental stage was tested using two-way ANOVA in the statistical software R.

Immunostaining

Embryonic lungs from ICR mice were washed with PBS and fixed with methanol for 30 min. Permeabilization was in 0.1% Triton X-100 for 30 min, followed by the blocking with 1.5% normal goat serum for 60 min. The samples were stained with anti-mouse E-cadherin monoclonal antibody ECCD-2 (1:100, Takara) for 16 h at 4°C, followed by washing three times with 0.1% Triton X-100 in PBS. After incubation with Alexa Fluor 488-conjugated goat anti-rat IgG secondary antibody (1:200, Thermo Fisher) for 30 min,

the sample was soaked in Sca*l*e reagent for tissue clearing overnight (37). The cell nuclei were stained with 5 μg/mL propidium iodide (PI; Dojindo).

Microscope observation

The lung explants were observed at 20x magnification using a Nikon C1 confocal microscope (Nikon Intech). Samples of live explants were kept in a stage-top chamber (Tokai Hit) to maintain a 5% CO_2 controlled atmosphere at 37°C for cellular homeostasis during the observation.

Particle cell model of the curvature-dependent growth

The steepness of $f(\xi)$ is determined by constants $c = 1.63$ and $\lambda = 2$ in Eq. 2. Parameter values $\gamma = 15$, $k_{\mathrm{c}} = 60$, $\hat{p} = 0.001$, and $\theta_{\mathrm{p}} = 0.2$ were used throughout the study. The other parameters are indicated in the figure legends.

Quadrilateral cell model of the cell shape regulation

The model framework we previously developed (34) was adapted to describe curvature-dependent growth (Figure 6). The forces applied to the apical (luminal side) and basal (outer side) vertices were modified as follows:

$$\begin{aligned} \mathbf{F}_i^{\mathrm{a}} &= \mathbf{f}_i^{\mathrm{a}} + \mathbf{f}_i^{\mathrm{sa}} + \mathbf{f}_i^{\mathrm{ab}} \\ \mathbf{F}_i^{\mathrm{b}} &= \mathbf{f}_i^{\mathrm{b}} + \mathbf{f}_i^{\mathrm{sb}} + \mathbf{f}_i^{\mathrm{ba}} + \mathbf{f}_i^{\mathrm{bend}} + \mathbf{f}_i^{\mathrm{w}} \quad , \end{aligned} \tag{13}$$

where $\mathbf{f}_i^{\mathrm{a}}$ and $\mathbf{f}_i^{\mathrm{sa}}$ are to approach the apical length and the cell area to the target values *a* and *s*, respectively (Figure 6A), and $\mathbf{f}_i^{\mathrm{ab}}$ is diagonal damper to prevent the cell from collapsing into a parallelogram. The corresponding forces $\mathbf{f}_i^{\mathrm{b}}$, $\mathbf{f}_i^{\mathrm{sb}}$, and $\mathbf{f}_i^{\mathrm{ba}}$ were applied to the basal vertex. The basal length regulation is as follows:

$$\mathbf{f}_i^{\mathrm{b}} = k_{\mathrm{b}} \left\{ (b - |\mathbf{b}_i - \mathbf{b}_{i-1}|) \frac{\mathbf{b}_i - \mathbf{b}_{i-1}}{|\mathbf{b}_i - \mathbf{b}_{i-1}|} + (b - |\mathbf{b}_i - \mathbf{b}_{i+1}|) \frac{\mathbf{b}_i - \mathbf{b}_{i+1}}{|\mathbf{b}_i - \mathbf{b}_{i+1}|} \right\} \tag{14}$$

where *b* is target value of the basal length. The apical length regulation was introduced in the same way. The cell area regulation was simplified with a coefficient $k_{\mathrm{s}} = 3$ as follows:

$$\mathbf{f}_i^{\mathrm{sb}} = -\mathbf{f}_i^{\mathrm{sa}} = k_{\mathrm{s}}(s - s_i) \frac{\mathbf{a}_i - \mathbf{b}_i}{|\mathbf{a}_i - \mathbf{b}_i|} \ . \tag{15}$$

The bending rigidity $\mathbf{f}_i^{\mathrm{bend}}$ in Eq. 3 was introduced only in the sequence of basal vertices to prevent the formation of a zigzag pattern (34). Vertex motion is expressed as follows:

$$\begin{aligned} \mathbf{a}_i^{t+1} &= \mathbf{a}_i^t + \gamma^{-1} \mathbf{F}_i^{\mathrm{a}} \Delta t \\ \mathbf{b}_i^{t+1} &= \mathbf{b}_i^t + \gamma^{-1} \mathbf{F}_i^{\mathrm{b}} \Delta t \ . \end{aligned} \tag{16}$$

For migration and cell division, tissue curvature estimation was performed by introducing φ_i, the angle between $\mathbf{x}_{i+3} - \mathbf{x}_i$ and $\mathbf{x}_i - \mathbf{x}_{i-3}$, to avoid detecting local

distortions. The target values of the apical length, basal length, and cell area of daughter cells were set to half those of the mother cell at cell division and fully grown for 50,000 time steps.

In Figure 6, we set $a = 0$, $b = 1$, and $s = 1$ and each cell shape was determined by the balance of the interactions. We used $k_{\mathrm{a}} = 0$ under the condition that apical constriction was not considered (Figure 6D) and $k_{\mathrm{a}} = 1$ to describe apical constriction (Figure 6E). The coefficients $k_{\mathrm{b}} = 300$ for $\mathbf{f}_i^{\mathrm{b}}$ and $k_{\mathrm{ab}} = 10$ for $\mathbf{f}_i^{\mathrm{ab}} = -\mathbf{f}_i^{\mathrm{ba}}$ were used. Note that $k_{\mathrm{bend}} = 0.2$ was used to make the cell shape uniform and hardly contributed to the bending rigidity of the tissue, which was due to cell shape regulation. The initial shape in Figure 6D and 6E was a thin tubular shape. The three vertices at the left end of each sequence were pinned at the initial positions, and no cell division occurred in the regions. The outer width of the pinned vertex region was 3. For protrusion growth, $k_{\mathrm{w}} = 1$, $\varphi_{\mathrm{w}} = 0.7, k_{\mathrm{q}} = 0.8$, and $\varphi_{\mathrm{q}} = 0.5$ were used.

In Figure 7, we used $k_{\mathrm{ab}} = 5$ and $k_{\mathrm{bend}} = 2$ for the very small cyst. Cell division was not assumed. Initially $k_{\mathrm{a}} = 0$ was set and increased by 0.003 at each time step until $k_{\mathrm{a}} = 3$.

Estimation of the shape transition of the elongated cyst model

Based on the model simulation in Figure 7A, we considered an elongated cyst shape in which the apical side forms an ellipse and the basal side is a combination of a rectangle with length x and semicircles with radius y. The longitudinal length of the cyst is $L = x + 2y$. It was assumed that the basal length and cell area are uniformly maintained as b

and s, respectively. The sum of the basal lengths of the cells is $bn = 2x + 2\pi y$. The apical lengths differ among cells, and the apical shape of the cyst is approximated to be an ellipse with major radius α and minor radius β. The apical length of the cell with the highest curvature is denoted by a_y. We assumed that $a_y/b = a_y/(y + x/2)$ holds by considering the cell shape as trapezoid with its sides radiating from the cyst center when intense apical constriction is exerted. The area of the cell is $s = (a_y + b)(y + x/2 - \alpha)/2$, and then we derived α as in Eq. 12. Additionally, the area of the elongated cyst was considered equal to that of the circular cyst, which can be written as $ns = 2xy + \pi y^2 - \pi\alpha\beta$. We then obtained β as in Eq. 12.

Integrated model of the cell type switching

The vertex motion is described as in the quadrilateral cell model, except that $\mathbf{f}_i^{\mathrm{w}}$ is replaced by $\mathbf{f}_i^{\mu}$. The initial shape was assumed to be the tip of an epithelial branch with a width of 10, in which 13 cells at the tip were assumed to be the tip type and the others were assumed to be the duct type. Cells at the proximal ends were pinned at their initial positions and no cell division was assumed in these cells. Apical length and cell area were assigned for the tip type (k_{at}, a_{t}, and s_{t}) and duct type (k_{ad}, a_{d}, and s_{d}), respectively. Parameter values $k_{\mathrm{ad}} = 40$, $a_{\mathrm{t}} = 0$, $k_{\mathrm{b}} = 300$, $k_{\mathrm{s}} = 50$, $s_{\mathrm{t}} = 1$, $s_{\mathrm{d}} = 2.7$, $k_{\mathrm{ab}} = 200$, and $k_{\mathrm{bend}} = 30$ were used. Other parameter values are indicated in the figure legends. Numerical calculations were performed until third-order branching emerged.

Numerical calculations

The time development of the models was calculated using C++ with $\Delta t = 0.005$, and the graphics were generated using *Mathematica*.

Results

Verification of the enhanced FGF10 signaling in protruded regions of lung epithelium

The assumption that the protruded region of the epithelium shows high growth activity is commonly required in theoretical models to reproduce branching patterns (12–14, 38). We examined extracellular signal-regulated kinase (ERK) activity as a hallmark of FGF receptor 2 (FGFR2) activation in embryonic mouse lungs (Figure 1 and S1). Lung explants from a transgenic mouse strain expressing a fluorescence resonance energy transfer (FRET) biosensor for ERK activity were used (36). To facilitate the laser light for FRET detection in the epithelium, we used a mesenchyme-free epithelium culture supplemented with recombinant FGF10 protein. Figure 1 shows the ERK activity map in the epithelium of the mouse lung at embryonic day 12.5 (E12.5), E13.5 and E14.5, which are the early pseudoglandular stage. It was demonstrated that ERK activity correlates with the cross-sectional curvature of the epithelial explants as $R^2 = 0.41$ in E12.5 and $R^2 = 0.45$ in E13.5, suggesting that FGF10 signaling was enhanced in protruded regions (Figure 1A and 1B). However, poor correlation and activation were observed in the E14.5 epithelium as $R^2 = 0.0031$ (Figure 1C). This result also excluded the possibility that the higher FRET signals at the protruded regions of the earlier explants were not due to differences in

detection efficiency. The linear regression analysis showed that the slopes of the signal to the curvature progressively declined as 6.18 (E12.5), 2.93 (E13.5), and 0.12 (E14.5). These results revealed that the signaling response of the epithelium to FGF10 is gradually attenuated with development, indicating the modification of epithelial properties during the developmental process.

We further examined whether the difference in ERK activity reflected its sensitivity to FGF10 concentration (Figure 2). Small explants (<100 μm) of the distal epithelium were grown in Matrigel with various concentrations of FGF10 for 18 h, and the ERK activity of each cyst was measured (Figure S2A). It was demonstrated that FGF10 enhanced ERK activity in a dose-dependent manner, with a correlation of $R^2 = 0.53$ (Figure 2A, black dots). E14.5 cysts showed a poor correlation with $R^2 = 0.013$ (Figure 2A, blue dots), which is consistent with Figure 1C. The slope of regression lines in E13.5 was significantly larger than in E14.5, with $P = 0.0014$, whereas the significant differences in intercepts were rejected, suggesting a higher dose dependency in E13.5 than in E14.5. ERK activation levels vary among cysts for the same FGF10 concentration and the same developmental stage, indicating that epithelial segments may have intrinsic FGF signaling reactivity.

These variations in ERK activity may be due to differences in FGF10-FGFR2 interaction. It was reported that FGF10 stimulates the internalisation of FGFR2 as early endosomes (39). Thus, we visualized FGF10 uptake into cells to observe receptor activation (Figure 2B). Epithelial explants were cultured with fluorescence-labeled FGF10 (FGF10-Alexa488) for 3 h, resulting in the appearance of small fluorescent

particles inside the cells (Figure S2B). Immunohistological analysis showed that FGF10 and FGFR2 localization overlapped with the fluorescent signals, suggesting that the signals reflected FGF10-Alexa488 uptake into cells by FGFR2 internalization (Figure S3). Unlike ERK activity, tissue curvature dependency of FGF10 uptake was not detected. The average fluorescent intensity of the explants showed a correlation with the FGF10 dose in E13.5 (R^2 = 0.87) and E14.5 (R^2 = 0.72), with slope 20.7 and 9.7, respectively (Figure 2B). These regression lines differed significantly $P = 1.2 \times 10^{-7}$. Collectively, these results suggest that epithelial responsiveness to FGF10 declines with the developmental stages in the lung epithelium, resulting in a difference in the activity gradient depending on the tissue curvature.

Mathematical model of the curvature-dependent epithelial growth

We considered that epithelial responsiveness to FGF10 may affect the branching pattern and examined this by constructing a mathematical model. The longitudinal section shape of the epithelial duct was described in a two-dimensional (2D) space by adopting a model framework, which we tentatively call the particle cell model, in which cells were assumed to be interacting particles (40–42). We aimed to represent the curvature-dependent growth process of the tissue in the simplest form, in which the FGF10 distribution and cell shape change were omitted.

The cell was assumed to be a uniform circular shape (Figure 3A) and to bind to its adjacent neighbours with a constant distance by introducing the distance-dependent interaction force (40, 41, 43) as follows,

$$\mathbf{f}_i^{\mathrm{c}} = k_{\mathrm{c}} \left\{ f\left(\frac{d_{i,i-1}}{\hat{d}_{i,i-1}}\right) \frac{\mathbf{x}_i - \mathbf{x}_{i-1}}{|\mathbf{x}_i - \mathbf{x}_{i-1}|} + f\left(\frac{d_{i,i+1}}{\hat{d}_{i,i+1}}\right) \frac{\mathbf{x}_i - \mathbf{x}_{i+1}}{|\mathbf{x}_i - \mathbf{x}_{i+1}|} \right\} , \tag{1}$$

$$f(\xi) = \begin{cases} \xi^{\lambda} + \left(\frac{c}{\xi}\right)^{\lambda} - 1 - c^{\lambda} & \text{for } 0 < \xi \leq 1 \\ \lambda\left(1 - c^{\lambda}\right)(\xi - 1) & \text{for } \xi > 1 \end{cases} , \tag{2}$$

where $\mathbf{f}_i^{\mathrm{c}}$ is the interaction force of the i-th cell with the (i-1)-th and (i+1)-th cells, k_{c} is the interaction strength, and $\mathbf{x}_i$ is a non-dimensionalized position vector of the i-th cell center. The cell-cell distance was given as $d_{i,j} = |\mathbf{x}_i - \mathbf{x}_j|$, and the optimal distance was $\hat{d}_{i,j} = r_i + r_j$ by introducing the cell radius r_i. The interaction $f(\xi)$ is attractive ($\xi > 1$) or repulsive ($\xi < 1$), depending on the relative distance (Figure 3B). The steepness of $f(\xi)$ is determined by constants c and λ (41).

The bending rigidity along the sequence of cells was introduced to express the smooth contours of the tissue as follows:

$$\mathbf{f}_i^{\mathrm{bend}} = k_{\mathrm{bend}} \left(\frac{\theta_i - \theta_{i-1}}{d_{i,i-1}} \mathbf{n}_{i-1,i} + \frac{\theta_i - \theta_{i+1}}{d_{i,i+1}} \mathbf{n}_{i,i+1} \right) , \tag{3}$$

where $\mathbf{f}_i^{\mathrm{bend}}$ and k_{bend} are the force and strength of bending rigidity, respectively; θ_i is the angle between the vectors $\mathbf{x}_i - \mathbf{x}_{i-1}$ and $\mathbf{x}_{i+1} - \mathbf{x}_i$, and $\mathbf{n}_{i-1,i}$ is the unit vector normal to the vector $\mathbf{x}_i - \mathbf{x}_{i-1}$ (π/2-rotation).

The position of the cell is changed according to the sum of the forces $\mathbf{F}_i = \mathbf{f}_i^{\mathrm{c}} + \mathbf{f}_i^{\mathrm{bend}}$ as follows:

$$\mathbf{x}_i^{t+1} = \mathbf{x}_i^t + \nu^{-1}\mathbf{F}_i \ \Delta t \quad , \tag{4}$$

where ν^{-1} corresponds to tissue shape plasticity, t is the time step, and Δt is the time-step size.

In addition to the above basic behavior, tissue growth was incorporated so that the protruded regions grow faster. We considered cell migration and division to be the factor of tissue growth, which depends on the local curvature (Figure 3C). This assumption is the phenomenological simplification of the diffusion-limited growth of epithelium, which has been described using reaction-diffusion (23, 44) or phase-field schemes (12, 45). In our model, cell migration is described as the outwards movement of each cell (Figure 3D) as follows:

$$\mathbf{f}_i^{\mathrm{m}} = \begin{cases} k_{\mathrm{m}}(\theta_i)^2\mathbf{n}_{i-1,i+1} & \text{for } \theta_i > 0 \\ 0 & \text{for } \theta_i \leq 0 \end{cases} \quad , \tag{5}$$

where $\mathbf{f}_i^{\mathrm{m}}$ is the migratory force, and k_{m} is the coefficient. The angle of cell sequence θ_i was used instead of calculating the local curvature (Figure 3C). The sum of the forces is expressed as follows:

$$\mathbf{F}_i \ = \mathbf{f}_i^{\mathrm{c}} + \mathbf{f}_i^{\mathrm{bend}} + \mathbf{f}_i^{\mathrm{m}} \quad . \tag{6}$$

Another source of tissue growth, cell division, was implemented by replacing a cell with two daughter cells with radius $r_i = r_0 = 0.1$, which gradually grew to the mother cell size $r_i = \hat{r} = 0.2$ in 1000 timesteps (Figure 3E). The cell divides with probability p_i between t and $t + \Delta t$ as follows:

$$p_i = \begin{cases} k_{\mathrm{p}}(\theta_i - \theta_{\mathrm{p}}) + \hat{p} & \text{for } \theta_i > \theta_{\mathrm{p}} \\ 0 & \text{for } \theta_i \leq \theta_{\mathrm{p}} \end{cases}, \tag{7}$$

where $\hat{p}$ is the basic probability and k_{p} and θ_{p} determine the magnitude of the shape dependency, assuming that cell division occurs only at the protruded regions.

The initial shape for the model simulation was assumed to be the tip of the epithelial branch (Figure 3F, left-most image). Ten cells at the proximal ends were pinned at their initial positions and no cell division was assumed for these cells. Our simple model of curvature-dependent growth explains the successive tip-splitting deformation (Figure 3F). Using this model, we examined how the shape dependency of growth, denoted by k_{m} and k_{p}, affects branch shape (Figure 3G). It was revealed that larger k_{m} and k_{p} values resulted in a longer segment length, suggesting that epithelial responsiveness to FGF10 determines the segment length during airway construction. When the shape dependency was high, a limited area at the branch tip showed high growth activity and tip elongation was facilitated instead of tip splitting. In contrast, in the case of low dependency, epithelial growth occurred in a wider area of the tip; therefore, tip expansion was promoted, causing shape instability owing to the reduced curvature. However, the branch

width did not differ significantly among the cases with different curvature dependencies, indicating that the whole mechanism of the hierarchy construction was not explained by the responsiveness change.

Contradiction between the segment length and width

Among the parameters in the model, the bending rigidity k_{bend} influenced the width (Figure 4). The higher rigidity of the epithelium generated a broader branch tip (Figure 4A), and this result is expected to be consistent in three-dimensional (3D) architecture (46). However, in the rigid epithelium condition, the segment length became shorter, revealing a contradiction to the actual airway structure in which the thicker airways have longer segment lengths. The broad tip easily induces shape instability under the assumption of curvature-dependent growth. The tip curvature was also lowered by increasing the width of the initial shape, and it was confirmed that the thicker branch segment became shorter (Figure 4B).

The property that potentially relates to bending rigidity is the cell shape (Figure 5) (34, 47). We observed the cell shape in the epithelial tip by E-cadherin staining and confirmed that the cells were larger at E12.5 than at E14.5 (Figure 5). The ratios of the lateral length to the basal length were 2.9 and 2.4 at E12.5 and E14.5, respectively (Figure 5G and 5H). It should be noted that the E13.5 cysts *in vitro* showed the tendency to be thicker than the E14.5 cyst (Figure S4A and S4C, blue solid line), indicating the change in the intrinsic property of the epithelium with development.

We examined how the cell shape affects the bending rigidity using another model

framework proposed in our previous study (Figure 6) (34, 48). Epithelial cell shape was described as a quadrilateral defined by four vertices (Figure 6A). Each cell is assumed to share two vertices with its adjacent cells, and the cell shape is controlled by the regulation of the basal length and cell area to be close to the prescribed target values. Apical and lateral lengths changed passively. Cell division was described by the addition of new vertices at the edges of the apical and basal sides (Figure 6B).

Using this model, the relationship between cell shape and tissue bending rigidity was examined, and it was found that a shorter basal length, accompanied by a longer lateral length, resulted in higher bending rigidity (Figure S5A and S5B). These results suggest that the thick epithelium in the early stage exhibits high bending rigidity, which gradually decreases during development. We again examined how the difference in cell shape results in curvature-dependent branch formation and confirmed that the thicker epithelium showed a shorter segment length (Figure S5C and S5D), consistent with Figure 4A. Thus, the high bending rigidity of the early tissue should reduce the branch scale, which is inconsistent with lung structure, and vice versa. (Figure S6). High response gain and tall cell shape were shown to be the hallmarks of early lung epithelium according to our observations, and they were suggested to contribute to making the branch segment longer and shorter, respectively, according to our model. Although it is not clear if the balance between the signal responsiveness and the cell shape could realize the hierarchical scaling of the branches along the developmental stage, the significant contrast between proximal and distal branches should require an additional mechanism that facilitates the formation of fine and short branches.

Mathematical model of apical constriction-induced branch formation

We have previously reported that the lung epithelium exhibits apical constriction and facilitates the formation of small buds through Wnt signaling (34). Inhibition of Wnt signaling has been shown to inhibit branching at the distal ends and to cause cystic expansion in murine lungs (29, 31). Based on these reports, we considered that apical constriction may be capable of facilitating tip splitting of fine distal branches (34). To investigate this concept, we examined the shape change of a growing epithelial branch under apical constriction (Figure 6).

Cell migration is described as the movement of vertices on the basal side represented by $\mathbf{f}_i^{\mathrm{w}}$, and cell division is described as the insertion of new vertices with probability q_i in each time step (Figure 6B). The dependency on the local curvature was assumed as follows:

$$\mathbf{f}_i^{\mathrm{w}} = \begin{cases} k_{\mathrm{w}} \varphi_i \mathbf{n}_{i-3,i+3} & \text{for } \varphi_i > \varphi_{\mathrm{w}} \\ 0 & \text{for } \varphi_i \leq \varphi_{\mathrm{w}} \end{cases}, \tag{8}$$

$$q_i = \begin{cases} k_{\mathrm{q}} \left(\varphi_i - \varphi_{\mathrm{q}} \right) & \text{for } \varphi_i > \varphi_{\mathrm{q}} \\ 0 & \text{for } \varphi_i \leq \varphi_{\mathrm{q}} \end{cases}, \tag{9}$$

where k_{w} and k_{q} denote the magnitude of the dependency, φ_i is the angle between $\mathbf{x}_{i+3} - \mathbf{x}_i$ and $\mathbf{x}_i - \mathbf{x}_{i-3}$, φ_{w} is the critical angle for migration, and φ_{q} is for cell division (see Materials and Methods and our previous study (34) for details). Apical constriction was implemented by applying an attractive force between the pair of apical

vertices with coefficient k_{a} (Figure 6C). For simplicity, all the cells were assumed to exhibit uniform apical constriction. Figure 6D and 6E show how branch elongation changed with and without apical constriction. Curvature-dependent growth promoted blanch elongation (Figure 6D) and apical constriction induced tip splitting (Figure 6E).

Mathematical analysis of the mechanical instability by cell shape regulation

We considered that apical constriction causes tip splitting due to mechanical instability caused by the imbalance between the increase in cell-autonomous curvature due to apical constriction and the decrease in tissue curvature due to growth (15, 34, 49). To understand the model dynamics, we examined the shape transition of model cysts consisting of 13–18 cells by introducing apical constriction (Figure 7). It was demonstrated that apical constriction transformed the cyst from a circular shape to an elongated shape if the cyst contained more than 15 cells; otherwise, the cyst sustained a circular shape (Figure 7A). The mechanical instability observed in this model represents the processes of bud formation in the epithelial cyst and tip splitting in the epithelial branch.

We explained how the number of cells determines whether the circular cyst will collapse by comparing the potential energy of the circular state, Ec and the elongated state, Ee (Figure 7B). The potential of the cyst was considered to comprise the regulation of the basal length, apical length, and cell area. If the basal length b and area s are sustained in the circular and elongated states, the difference in the potential $Ec - Ee$ is derived by comparing the apical lengths of the cysts as follows:

$$Ec - Ee = \sum_{i}^{n} c_i k_{\mathrm{a}} - \sum_{i}^{n} e_i k_{\mathrm{a}} = k_a \left(nc_i - \sum_{i}^{n} e_i \right) , \tag{10}$$

where n is the number of cells, k_{a} is the strength of apical constriction, and c_i and e_i is the apical lengths of the i-th cell in the circular and elongated cysts, respectively. We used $k_{\mathrm{b}} = 300$, which strongly regulates the basal length to be the target value b in the model cell. Then the sum of the apical length of the circular cyst is approximated as $nc_i \sim \sqrt{n^2 b^2 - 4\pi ns}$ by assuming if the basal and apical sides form arcs. For the elongated cyst, we assumed that the apical side forms an ellipse according to the model shapes in Figure 7A; therefore, the total apical length of the elongated cyst was approximated as follows:

$$\sum_{i}^{n} e_i \sim \int_0^{2\pi} \sqrt{\alpha^2 - (\alpha^2 - \beta^2) \sin^2 x}\, dx \ , \tag{11}$$

where α and β are the major and minor radii of an ellipse, respectively. We estimated α and β by considering the conservation of cell areas and the relationship between cell height and apical length, as follows:

$$\begin{aligned} \alpha &= \frac{\sqrt{bL^2 - 4s}}{2\sqrt{b}} \\ \beta &= \frac{(bn - 2L)\big((\pi - 4)bn + 2L\pi\big) - 4ns(\pi - 2)^2}{4\pi\alpha(\pi - 2)^2} \ , \end{aligned} \tag{12}$$

where L is the major axis length of the cyst, which was introduced to define cyst shape.

Figure 7B shows the numerical profile of $Ec - Ee$ against L for n ranging from 13 to 18. The range of n should be $n > 12$ when $b = s = 1$, such that $n^2b^2 - 4\pi ns > 0$ holds. The minimum of L is bn/π, which corresponds to the case of a circular cyst. The maximum of $Ec - Ee$ indicates the most stable shape with apical constriction, and this estimation was found to be consistent with the model simulation in Figure 7A. Figure 7C shows the estimation of the cyst axes with respect to the number of cells, indicating that the minor axis does not exceed the radius of the circular cyst. These calculations do not consider more complex deformation other than elongation, however, they can be used to estimate the destabilization of the circular cyst state. The minor axis characterizes the appropriate branch radius corresponding to the cell-autonomous curvature under apical constriction. In this regard, we collected the minimum minor axis length for any cell numbers and found that it decreases with b/s regardless of s (Figure 7D). Although the cell size affects the critical cell number for shape transition (Figure 7E), the stable branch width is determined only by the cell shape (Figure 7D). These results suggest that apical constriction effectively induces deformation in the epithelium comprising flattened cells compared to thicker cells. Consequently, the model analysis indicated the possibility that the involvement of apical constriction counteracts the effect of the mechanical properties of the epithelium caused by the cell height change and achieves the hierarchical structure.

Coordination of curvature-dependent growth and apical constriction

Although we assumed that apical constriction exerts a force that promotes tissue-level deformation in Figure 7, it is unlikely that Wnt-induced apical constriction occurs in the entire lung epithelium. It has been shown that canonical Wnt signaling is more intense in the tip region of the lung epithelium (50, 51). Sox2, which is inhibited by the Wnt/b-catenin pathway, is expressed on the duct side, exhibiting exclusive localization with Sox9 expression, which is enhanced by Wnt signaling on the tip side (52). This suggests that the cells at the tip and duct are under distinct signaling regimes. Figure 8A demonstrates that the thickness of the epithelium differs between the tip and duct. This result is consistent with the results of a detailed 3D analysis of cell shape in which elongated columnar cells were observed at the stalk region and short columnar cells were observed at the developing bud tip in the lungs of E11.5 mice (35). In our observations, cells in the concave region were also thickened, suggesting that cells may undergo specification of the duct accompanied by cell elongation. Corresponding results were shown in the lung cyst culture, which indicates the tendency of higher curvature explants to show thinner epithelia and that FGF10 makes epithelia thinner (Figure S4B and S4C, blue solid line).

Based on these insights, we constructed an integrated model, in which tissue growth and apical constriction occur only at the tip. It was assumed that the switching of the cell behavior from the tip type (small cells with apical constriction) to the duct type (large columnar cells with no apical constriction) depending on the local tissue curvature (Figure 8B). In the implementation, the cell is initially of the tip type and switches to the duct

type when $\varphi_i > \varphi_{\mathrm{d}}$. The critical angle for switching φ_{d} represents the response gain depending on the tissue curvature. Tissue growth in the high curvature area was described by migration and cell division specific for the tip type cells. Migration was described by moving the basal vertex with force $\mathbf{f}_i^{\mu} = k_{\mu}\mathbf{n}_{i-3,i+3}$, which was replaced with $\mathbf{f}_i^{\mathrm{w}}$ in Eq. 8. Cell division occurs with probability ρ. The model dynamics were described as in the quadrilateral cell model, except that distinct values were assigned for the tip and duct types.

Figure 8C shows the higher-order branching process reproduced by the integrated model. Tall cells with a high response gain resulted in a larger-scale branching structure, compared to the case of shorter cells (Figure S7A). When the curvature dependency was lowered to depict branching in the later phase, the segment length was reduced (Figure S7B), consistent with the results in the particle cell model in Figure 3G. When the reduced cell height was assumed, which corresponds to the later phase, then the segment length is reduced again (Figure 8D). This condition results in a widened tip. When we assumed intensive apical constriction, in addition to flat cells with a lower response gain, thin and short branches were formed (Figure 8E). Apical constriction has a greater impact on branching shapes in the case of flatter cells than taller cells (the comparison of Figure 8D and 8E versus the comparison of Figure S7B and S7C), as flatter cells have a wider range of possible local curvatures. The integrated model indicates that curvature dependence in growth response and cell flattening, with the help of apical constriction, can control the branch scale (Figure 8F).

Discussion

Early mathematical modeling studies addressed lung epithelial morphogenesis dependent on extrinsic FGF10 distribution based on the importance of signaling molecules regulated by reciprocal interactions between the epithelium and mesenchyme in airway structure formation (12, 14, 23, 38). Subsequently, it was revealed that FGF10 expression patterns in the lung mesenchyme were not required for epithelial branching (53), triggering the hypothesis of an epithelium-autonomous deformation mechanism using a combined experimental and theoretical approach (15, 16, 34). Epithelial buckling and apical constriction explain epithelial bud formation but are not related to the mechanism of branch elongation, which may require intensive growth in the protruded region. We experimentally demonstrated that epithelial growth, represented by ERK activity, correlated to the tissue curvature (Figure 1) and modeled higher-order branch formation by phenomenologically incorporating curvature-dependent growth (Figure 3). Previous mathematical modeling studies have shown the possibility of enhancing signal intensity at epithelial protrusions by describing diffuse molecular interactions that depend on the tissue geometry (12, 13, 54). However, the conditions for generating patterns by molecular interactions are restricted, and the branching interval has not been well investigated to date. Our simple model reveals the conditions that modify the branching intervals to achieve a hierarchical structure of the lung.

How a specific outgrowth at the epithelial protrusion is regulated remains an important unsolved issue. In addition to the molecular interactions, an effect of geometry-dependent mechanical patterning should be considered. When human embryonic stem

cell-derived lung epithelial progenitor cells were cultured in tube geometry, SOX2 expression was suppressed via canonical Wnt signaling, whereas SOX9 expression was maintained (52). Such differential expression was observed at a tube diameter of 100 μm, but not at 400 μm. The fact that the expression of distal and proximal markers was regulated depending on the tissue curvature indicates the contribution of mechanotransduction by geometry-dependent tension. Mouse lungs genetically deficient in epithelial YAP, a mediator of Hippo signaling, have been shown to become cystic without branching, supporting the crucial role of mechanical signaling during lung development (55). YAP is also required for the differentiation of smooth muscle covering the epithelium, depending on luminal pressure (56).

Smooth muscle that wraps the lung epithelium is thought to mediate duct diameter (57) and promote tip splitting by sculpting the cleft in the epithelial bud tip (58), which is still controversial (56, 57). The active involvement of smooth muscle in morphogenesis has not been demonstrated in organs with randomly branched elongated serpentine ducts, such as the pancreas, mammary gland, and thyroid gland (59–61), suggesting that the regularly branching structure from the widened lumen is characteristic of the airways sculpted by smooth muscle differentiation. In our model, ducts and clefts are described by introducing curvature-dependent cell-shape switching. Further analysis of the correlations and causal relationships among smooth muscle formation, cell shape changes, and curvature of the epithelial tissue should be performed.

The lung epithelium secretes fluid into the lumen, and luminal flow has been observed in cultures of E11 mouse lung (62, 63). The role of luminal flow in

morphogenesis has been reported in *ex vivo* cultures of E12 mouse lungs, where artificial pressure application promotes growth, and decompression inhibits branching (64, 65). If we consider that luminal pressure pushes the lung epithelium outwards, this effect can be considered analogous to the increase in bending rigidity in our model (Figure 4A and S6), and the result that higher rigidity promotes branching is consistent with those studies. Our model also demonstrated that bending rigidity widened the tip (Figure 4A and S6), which might not be linked to the mechanism that controls the duct diameter in a 3D space, while it may be consistent that wider ducts are composed of a thicker epithelium. In association with the proximal duct being covered with smooth muscle, inhibition of smooth muscle differentiation by myocardin gene knockout reduced the size of the lumen (57). It was also reported that mutational activation of RAS, a critical effector of ERK, controls mitotic spindle orientation in epithelium and consequently affects the thickness to length ratio of the early lung epithelium, independently of proliferative activity and cell shape changes (66). As this report suggested the involvement of planar cell polarity (PCP) in controlling duct shape, subsequent experimental studies have indicated that PCP components affect lung epithelial morphology (67–70). The components of the PCP pathway are involved in Wnt signaling-mediated cytoskeletal regulation, directing cell shape changes and migration (71). Since Wnt, Hippo, and FGF signaling are interrelated to control lung morphology (72), it is difficult to unravel how they regulate tip shape, branch formation, and duct shape. In this study, we propose the potential significance of apical constriction, cell size, and shape change in the emergence of hierarchical lung morphology.

Conclusion

We proposed regulatory mechanisms to generate a hierarchical structure of the lung airways. By focusing on epithelial properties, we experimentally showed that FGF10 responsiveness of the epithelium changes with development, and theoretically demonstrated that this leads to differences in the branch segment length under the assumption of curvature-dependent growth. In addition, we proposed apical constriction-induced branch formation, which is predicted to be necessary for the formation of short and thin branches in the distal airway. Our analysis indicated that the effectiveness of apical constriction depends on cell shape, resulting in an intensified structural hierarchy in the lung airways. This theoretical prediction suggests the significance of Wnt in regulating epithelial cell shape during the developmental stages of lung structure regulation. Taken together, this study provides a new perspective on how epithelial properties regulate the mesoscale branching structure of the lung.

Limitations of the Study

Our observations and modeling were performed in a 2D plane. The relationship between tissue curvature and ERK activity in the lung epithelial tissue was determined for the observed cross section, and we could not quantify curvature in three dimensions. The model does not represent a 3D structure and might be not suitable for discussing the lumen diameter of the duct. Epithelial tissues grow in directions that do not collide with each other in the lung, however, this effect was not considered. The involvement of the

mesenchyme, such as the concentration gradient of FGF10 and formation of smooth muscle, was not represented in the model.

Author Contributions

H.T.-I. designed research, performed experimental and theoretical research, constructed models, and wrote the manuscript; H.T. executed experiments and analyzed data; T. M. supervised research. All authors have read and approved the published manuscript.

Declaration of Interests

The authors declare no competing interests.

Acknowledgement

The authors thank Dr. Katsumi Fumoto (Osaka University) for his helpful discussions. We thank Prof. Michiyuki Matsuda (Kyoto University) for the use of Eisuke transgenic mice. We thank Ms. Yoshimi Yamaguchi for technical assistance with the FGF10 labeling experiment. This work was supported by JSPS KAKENHI Grant Number 18K06260 (H.T.-I.) and 15KT0018 (T.M).

Reference

1. Boyden, E.A. 1961. The Nomenclature of the Bronchopulmonary Segments and Their Blood Supply. *Dis. Chest*. 39:1–6, doi: 10.1378/chest.39.1.1.
2. Jackson, C.L., and J.F. Huber. 1943. Correlated Applied Anatomy of the

Bronchial Tree and Lungs With a System of Nomenclature. *Dis. Chest*. 9:319–326, doi: 10.1378/chest.9.4.319.

3. Fujii, S., T. Muranaka, J. Matsubayashi, S. Yamada, A. Yoneyama, and T. Takakuwa. 2021. Bronchial tree of the human embryo: Categorization of the branching mode as monopodial and dipodial. *PLoS One*. 16:1–13, doi: 10.1371/journal.pone.0245558.
4. Metzger, R.J., O.D. Klein, G.R. Martin, and M.A. Krasnow. 2008. The branching programme of mouse lung development. *Nature*. 453:745–750, doi: 10.1038/nature07005.
5. Jones, M.R., L. Chong, and S. Bellusci. 2021. Fgf10/Fgfr2b Signaling Orchestrates the Symphony of Molecular, Cellular, and Physical Processes Required for Harmonious Airway Branching Morphogenesis. *Front. Cell Dev. Biol.* 8:1–24, doi: 10.3389/fcell.2020.620667.
6. Glenny, R.W., M. Krueger, C. Bauer, and R.R. Beichel. 2020. The fractal geometry of bronchial trees differs by strain in mice. *J. Appl. Physiol.* 128:362–367, doi: 10.1152/japplphysiol.00838.2019.
7. Counter, W.B., I.Q. Wang, T.H. Farncombe, and N.R. Labiris. 2013. Airway and pulmonary vascular measurements using contrast-enhanced micro-CT in rodents. *Am. J. Physiol. - Lung Cell. Mol. Physiol.* 304:831–843, doi: 10.1152/ajplung.00281.2012.
8. Tawhai, M.H., P. Hunter, J. Tschirren, J. Reinhardt, G. McLennan, and E.A. Hoffman. 2004. CT-based geometry analysis and finite element models of the human and ovine bronchial tree. *J. Appl. Physiol.* 97:2310–2321, doi: 10.1152/japplphysiol.00520.2004.
9. Nelson, T., B. West, and A. Goldberger. 1990. The fractal lung: Universal and species-related scaling patterns. *Experientia*. 46:251–254.
10. Nogawa, H., K. Morita, and W. V. Cardoso. 1998. Bud formation precedes the appearance of differential cell proliferation during branching morphogenesis of mouse lung epithelium in vitro. *Dev. Dyn.* 213:228–235, doi: 10.1002/(SICI)1097-0177(199810)213:2<228::AID-AJA8>3.0.CO;2-I.
11. Bellusci, S., J. Grindley, H. Emoto, N. Itoh, and B.L.M. Hogan. 1997. Fibroblast Growth Factor 10 (FGF10) and branching morphogenesis in the embryonic mouse lung. *Development*. 124:4867–4878, doi: 10.1242/dev.124.23.4867.

12. Clément, R., P. Blanc, B. Mauroy, V. Sapin, and S. Douady. 2012. Shape Self-Regulation in Early Lung Morphogenesis. *PLoS One*. 7:e36925, doi: 10.1371/journal.pone.0036925.
13. Miura, T., and K. Shiota. 2000. Time-lapse observation of branching morphogenesis of the lung bud epithelium in mesenchyme-free culture and its relationship with the localization of actin filaments. *Int. J. Dev. Biol.* 44:899–902.
14. Menshykau, D., C. Kraemer, and D. Iber. 2012. Branch mode selection during early lung development. *PLoS Comput. Biol.* 8, doi: 10.1371/journal.pcbi.1002377.
15. Kim, H.Y., V.D. Varner, and C.M. Nelson. 2013. Apical constriction initiates new bud formation during monopodial branching of the embryonic chicken lung. *Dev.* 140:3146–3155, doi: 10.1242/dev.093682.
16. Varner, V.D., J.P. Gleghorn, E. Miller, D.C. Radisky, and C.M. Nelson. 2015. Mechanically patterning the embryonic airway epithelium. *Proc. Natl. Acad. Sci. U. S. A.* 112:9230–9235, doi: 10.1073/pnas.1504102112.
17. Iber, D. 2021. The control of lung branching morphogenesis. *Curr. Top. Dev. Biol.* 143:205–237, doi: 10.1016/bs.ctdb.2021.02.002.
18. Volckaert, T., and S.P. De Langhe. 2015. Wnt and FGF mediated epithelial-mesenchymal crosstalk during lung development. *Dev. Dyn.* 244:342–366, doi: 10.1002/dvdy.24234.
19. Weaver, M., N.R. Dunn, and B.L.M. Hogan. 2000. Bmp4 and Fgf10 play opposing roles during lung bud morphogenesis. *Development*. 127:2695–2704, doi: 10.1242/dev.127.12.2695.
20. Abler, L.L., S.L. Mansour, and X. Sun. 2008. Conditional gene inactivation reveals roles for Fgf10 and Fgfr2 in establishing a normal pattern of epithelial branching in the mouse lung. *Dev. Dyn.* 238:1999–2013, doi: 10.1002/dvdy.22032.
21. Bellusci, S., Y. Furuta, M.G. Rush, R. Henderson, G. Winnier, and B.L.M. Hogan. 1997. Involvement of Sonic hedgehog (Shh) in mouse embryonic lung growth and morphogenesis. *Development*. 124:53–63, doi: 10.1242/dev.124.1.53.
22. Pepicelli, C. V., P.M. Lewis, and A.P. McMahon. 1998. Sonic hedgehog regulates branching morphogenesis in the mammalian lung. *Curr. Biol.* 8:1083–

1086, doi: 10.1016/S0960-9822(98)70446-4.

23. Miura, T., and K. Shiota. 2002. Depletion of FGF acts as a lateral inhibitory factor in lung branching morphogenesis in vitro. *Mech. Dev.* 116:29–38, doi: 10.1016/S0925-4773(02)00132-6.

24. Matsushita, M., J. Wakita, H. Itoh, I. Ràfols, T. Matsuyama, H. Sakaguchi, and M. Mimura. 1998. Interface growth and pattern formation in bacterial colonies. *Phys. A Stat. Mech. its Appl.* 249:517–524, doi: 10.1016/S0378-4371(97)00511-6.

25. Ben-Jacob, E., H. Shmueli, O. Shochet, and A. Tenenbaum. 1992. Adaptive self-organization during growth of bacterial colonies. *Phys. A Stat. Mech. its Appl.* 187:378–424, doi: 10.1016/0378-4371(92)90002-8.

26. Daccord, G., J. Nittmann, S. Etienne, and H.E. Stanley. 1986. Radial viscous fingers and diffusion-limited aggregation: Fractal dimension and growth sites. *Phys. Rev. Lett.* 56:336–339.

27. Yokoyama, E., and T. Kuroda. 1990. Pattern formation in growth of snow crystals occurring in the surface kinetic process and the diffusion process. *Phys. Rev. A*. 41:2038–2049, doi: 10.1103/PhysRevA.41.2038.

28. Lubkin, S.R., and J.D. Murray. 1995. A mechanism for early branching in lung morphogenesis. *J. Math. Biol.* 34:77–94, doi: 10.1007/BF00180137.

29. Mucenski, M.L., S.E. Wert, J.M. Nation, D.E. Loudy, J. Huelsken, W. Birchmeier, E.E. Morrisey, and J.A. Whitsett. 2003. B-Catenin Is Required for Specification of Proximal/Distal Cell Fate During Lung Morphogenesis. *J. Biol. Chem.* 278:40231–40238, doi: 10.1074/jbc.M305892200.

30. Shu, W., S. Guttentag, Z. Wang, T. Andl, P. Ballard, M.M. Lu, S. Piccolo, W. Birchmeier, J.A. Whitsett, S.E. Millar, et al. 2005. Wnt/β-catenin signaling acts upstream of N-myc, BMP4, and FGF signaling to regulate proximal-distal patterning in the lung. *Dev. Biol.* 283:226–239, doi: 10.1016/j.ydbio.2005.04.014.

31. Goss, A.M., Y. Tian, T. Tsukiyama, E.D. Cohen, D. Zhou, M.M. Lu, T.P. Yamaguchi, and E.E. Morrisey. 2009. Wnt2/2b and β-Catenin Signaling Are Necessary and Sufficient to Specify Lung Progenitors in the Foregut. *Dev. Cell*. 17:290–298, doi: 10.1016/j.devcel.2009.06.005.

32. Hrycaj, S.M., B.R. Dye, N.C. Baker, B.M. Larsen, A.C. Burke, J.R. Spence, and

D.M. Wellik. 2015. Hox5 genes regulate the Wnt2/2b-Bmp4-signaling axis during lung development. *Cell Rep.* 12:903–912, doi: 10.1016/j.celrep.2015.07.020.

33. Lüdtke, T.H., C. Rudat, I. Wojahn, A.C. Weiss, M.J. Kleppa, J. Kurz, H.F. Farin, A. Moon, V.M. Christoffels, and A. Kispert. 2016. Tbx2 and Tbx3 Act Downstream of Shh to Maintain Canonical Wnt Signaling during Branching Morphogenesis of the Murine Lung. *Dev. Cell*. 39:239–253, doi: 10.1016/j.devcel.2016.08.007.
34. Fumoto, K., H. Takigawa-Imamura, K. Sumiyama, T. Kaneiwa, and A. Kikuchi. 2017. Modulation of apical constriction by Wnt signaling is required for lung epithelial shape transition. *Dev.* 144:151–162, doi: 10.1242/dev.141325.
35. Kadzik, R.S., E.D. Cohen, M.P. Morley, K.M. Stewart, M.M. Lu, and E.E. Morrisey. 2014. Wnt ligand/Frizzled 2 receptor signaling regulates tube shape and branch-point formation in the lung through control of epithelial cell shape. *Proc. Natl. Acad. Sci. U. S. A.* 111:12444–12449, doi: 10.1073/pnas.1406639111.
36. Kamioka, Y., K. Sumiyama, R. Mizuno, Y. Sakai, E. Hirata, E. Kiyokawa, and M. Matsuda. 2012. Live imaging of protein kinase activities in transgenic mice expressing FRET biosensors. *Cell Struct. Funct.* 37:65–73, doi: 10.1247/csf.11045.
37. Hama, H., H. Kurokawa, H. Kawano, R. Ando, T. Shimogori, H. Noda, K. Fukami, A. Sakaue-Sawano, and A. Miyawaki. 2011. Scale: A chemical approach for fluorescence imaging and reconstruction of transparent mouse brain. *Nat. Neurosci.* 14:1481–1488, doi: 10.1038/nn.2928.
38. Hirashima, T., Y. Iwasa, and Y. Morishita. 2009. Mechanisms for split localization of Fgf10 expression in early lung development. *Dev. Dyn.* 238:2813–2822, doi: 10.1002/dvdy.22108.
39. Francavilla, C., K.T.G. Rigbolt, K.B. Emdal, G. Carraro, E. Vernet, D.B. Bekker-Jensen, W. Streicher, M. Wikström, M. Sundström, S. Bellusci, et al. 2013. Functional Proteomics Defines the Molecular Switch Underlying FGF Receptor Trafficking and Cellular Outputs. *Mol. Cell*. 51:707–722, doi: 10.1016/j.molcel.2013.08.002.
40. Takigawa-Imamura, H., R. Morita, T. Iwaki, T. Tsuji, and K. Yoshikawa. 2015. Tooth germ invagination from cell-cell interaction: Working hypothesis on

mechanical instability. *J. Theor. Biol.* 382:284–291, doi: 10.1016/j.jtbi.2015.07.006.

41. Higaki, T., H. Takigawa-Imamura, K. Akita, N. Kutsuna, R. Kobayashi, S. Hasezawa, and T. Miura. 2017. Exogenous cellulase switches cell interdigitation to cell elongation in an RIC1-dependent manner in Arabidopsis thaliana cotyledon pavement cells. *Plant Cell Physiol.* 58:106–119, doi: 10.1093/pcp/pcw183.
42. Hirano, T., H. Konno, S. Takeda, L. Dolan, M. Kato, T. Aoyama, T. Higaki, H. Takigawa-Imamura, and M.H. Sato. 2018. PtdIns(3,5)P2 mediates root hair shank hardening in Arabidopsis. *Nat. Plants*. 4:888–897, doi: 10.1038/s41477-018-0277-8.
43. Gunji, S., Y. Oda, H. Takigawa-Imamura, H. Tsukaya, and A. Ferjani. 2020. Excess Pyrophosphate Restrains Pavement Cell Morphogenesis and Alters Organ Flatness in Arabidopsis thaliana. *Front. Plant Sci.* 11, doi: 10.3389/fpls.2020.00031.
44. Hartmann, D., and T. Miura. 2006. Modelling in vitro lung branching morphogenesis during development. *J. Theor. Biol.* 242:862–872, doi: 10.1016/j.jtbi.2006.05.009.
45. George, U.Z., K.K. Bokka, D. Warburton, and S.R. Lubkin. 2015. Quantifying stretch and secretion in the embryonic lung: Implications for morphogenesis. *Mech. Dev.* 138:356–363, doi: 10.1016/j.mod.2015.07.003.
46. Boudon, F., J. Chopard, O. Ali, B. Gilles, O. Hamant, A. Boudaoud, J. Traas, and C. Godin. 2015. A Computational Framework for 3D Mechanical Modeling of Plant Morphogenesis with Cellular Resolution. *PLoS Comput. Biol.* 11, doi: 10.1371/journal.pcbi.1003950.
47. Štorgel, N., M. Krajnc, P. Mrak, J. Štrus, and P. Ziherl. 2016. Quantitative Morphology of Epithelial Folds. *Biophys. J.* 110:269–277, doi: 10.1016/j.bpj.2015.11.024.
48. Fumoto, K., H. Takigawa-Imamura, K. Sumiyama, S.H. Yoshimura, N. Maehara, and A. Kikuchi. 2019. Mark1 regulates distal airspace expansion through type I pneumocyte flattening in lung development. *J. Cell Sci.* 132, doi: 10.1242/jcs.235556.
49. Bar-ziv, R., and E. Moses. 1994. Instability and “pearling” states produced in

tubular membranes by competition of curvature and tension. *Phys. Rev. Lett.* 73:1392–1395.

50. De Langhe, S.P., F.G. Sala, P.M. Del Moral, T.J. Fairbanks, K.M. Yamada, D. Warburton, R.C. Burns, and S. Bellusci. 2005. Dickkopf-1 (DKK1) reveals that fibronectin is a major target of Wnt signaling in branching morphogenesis of the mouse embryonic lung. *Dev. Biol.* 277:316–331, doi: 10.1016/j.ydbio.2004.09.023.
51. Yin, Y., A.C. White, S.H. Huh, M.J. Hilton, H. Kanazawa, F. Long, and D.M. Ornitz. 2008. An FGF-WNT gene regulatory network controls lung mesenchyme development. *Dev. Biol.* 319:426–436, doi: 10.1016/j.ydbio.2008.04.009.
52. Soleas, J.P., E. D'Arcangelo, L. Huang, G. Karoubi, M.C. Nostro, A.P. McGuigan, and T.K. Waddell. 2020. Assembly of lung progenitors into developmentally-inspired geometry drives differentiation via cellular tension. *Biomaterials*. 254:120128, doi: 10.1016/j.biomaterials.2020.120128.
53. Volckaert, T., A. Campbell, E. Dill, C. Li, P. Minoo, and S. De Langhe. 2013. Localized Fgf10 expression is not required for lung branching morphogenesis but prevents differentiation of epithelial progenitors. *Dev.* 140:3731–3742, doi: 10.1242/dev.096560.
54. Menshykau, D., P. Blanc, E. Unal, V. Sapin, and D. Iber. 2014. An interplay of geometry and signaling enables robust lung branching morphogenesis. *Dev.* 141:4526–4536, doi: 10.1242/dev.116202.
55. Lin, C., E. Yao, K. Zhang, X. Jiang, S. Croll, K. Thompson-Peer, and P.T. Chuang. 2017. YAP is essential for mechanical force production and epithelial cell proliferation during lung branching morphogenesis. *Elife*. 6:1–25, doi: 10.7554/eLife.21130.
56. Jaslove, J.M., K. Goodwin, A. Sundarakrishnan, J.W. Spurlin, S. Mao, A. Košmrlj, and C.M. Nelson. 2022. Transmural pressure signals through retinoic acid to regulate lung branching. *Dev.* 149, doi: 10.1242/dev.199726.
57. Young, R.E., M.K. Jones, E.A. Hines, R. Li, Y. Luo, W. Shi, J.M. Verheyden, and X. Sun. 2020. Smooth Muscle Differentiation Is Essential for Airway Size, Tracheal Cartilage Segmentation, but Dispensable for Epithelial Branching. *Dev. Cell*. 53:73-85.e5, doi: 10.1016/j.devcel.2020.02.001.
58. Kim, H.Y., M.F. Pang, V.D. Varner, L. Kojima, E. Miller, D.C. Radisky, and

C.M. Nelson. 2015. Localized Smooth Muscle Differentiation Is Essential for Epithelial Bifurcation during Branching Morphogenesis of the Mammalian Lung. *Dev. Cell*. 34:719–726, doi: 10.1016/j.devcel.2015.08.012.

59. Dahl-Jensen, S.B., S. Yennek, L. Flasse, H.L. Larsen, D. Sever, G. Karremore, I. Novak, K. Sneppen, and A. Grapin-Botton. 2018. Deconstructing the principles of ductal network formation in the pancreas. *PLoS Biol.* 16:1–25, doi: 10.1371/journal.pbio.2002842.
60. Liang, S., E. Johansson, G. Barila, D.L. Altschuler, H. Fagman, and M. Nilsson. 2018. A branching morphogenesis program governs embryonic growth of the thyroid gland. *Dev.* 145, doi: 10.1242/dev.146829.
61. Scheele, C.L.G.J., E. Hannezo, M.J. Muraro, A. Zomer, N.S.M. Langedijk, A. Van Oudenaarden, B.D. Simons, and J. Van Rheenen. 2017. Identity and dynamics of mammary stem cells during branching morphogenesis. *Nature*. 542:313–317, doi: 10.1038/nature21046.
62. Schittny, J.C., G. Miserocchi, and M.P. Sparrow. 2000. Spontaneous peristaltic airway contractions propel lung liquid through the bronchial tree of intact and fetal lung explants. *Am. J. Respir. Cell Mol. Biol.* 23:11–18, doi: 10.1165/ajrcmb.23.1.3926.
63. Olver, R.E., D. V. Walters, and S.M. Wilson. 2004. Developmental regulation of lung liquid transport. *Annu. Rev. Physiol.* 66:77–101, doi: 10.1146/annurev.physiol.66.071702.145229.
64. Nelson, C.M., J.P. Gleghorn, M.F. Pang, J.M. Jaslove, K. Goodwin, V.D. Varner, E. Miller, D.C. Radisky, and H.A. Stone. 2017. Microfluidic chest cavities reveal that transmural pressure controls the rate of lung development. *Dev.* 144:4328–4335, doi: 10.1242/dev.154823.
65. Stanton, A.E., K. Goodwin, A. Sundarakrishnan, J.M. Jaslove, J.P. Gleghorn, A.L. Pavlovich, and C.M. Nelson. 2021. Negative Transpulmonary Pressure Disrupts Airway Morphogenesis by Suppressing Fgf10. *Front. Cell Dev. Biol.* 9:1–15, doi: 10.3389/fcell.2021.725785.
66. Tang, N., W.F. Marshall, M. McMahon, R.J. Metzger, and G.R. Martin. 2011. Control of mitotic spindle angle by the RAS-regulated ERK1/2 pathway determines lung tube shape. *Science (80-.).* 333:342–345, doi: 10.1126/science.1204831.

67. Zhang, K., E. Yao, E. Chuang, B. Chen, E.Y. Chuang, R.F. Volk, K.L. Hofmann, B. Zaro, and P.T. Chuang. 2022. Wnt5a-Vangl1/2 signaling regulates the position and direction of lung branching through the cytoskeleton and focal adhesions. *PLoS Biol.* 20, doi: 10.1371/journal.pbio.3001759.
68. Yates, L.L., C. Schnatwinkel, L. Hazelwood, L. Chessum, A. Paudyal, H. Hilton, M.R. Romero, J. Wilde, D. Bogani, J. Sanderson, et al. 2013. Scribble is required for normal epithelial cell-cell contacts and lumen morphogenesis in the mammalian lung. *Dev. Biol.* 373:267–280, doi: 10.1016/j.ydbio.2012.11.012.
69. Yates, L.L., C. Schnatwinkel, J.N. Murdoch, D. Bogani, C.J. Formstone, S. Townsend, A. Greenfield, L.A. Niswander, and C.H. Dean. 2010. The PCP genes Celsr1 and Vangl2 are required for normal lung branching morphogenesis. *Hum. Mol. Genet.* 19:2251–2267, doi: 10.1093/hmg/ddq104.
70. Gegg, M., A. Böttcher, I. Burtscher, S. Hasenoeder, C. Van Campenhout, M. Aichler, A. Walch, S.G.N. Grant, and H. Lickert. 2014. Flattop regulates basal body docking and positioning in mono- and multiciliated cells. *Elife*. 3:1–24, doi: 10.7554/eLife.03842.
71. Cheong, S.S., K.M. Akram, C. Matellan, S.Y. Kim, D.C.A. Gaboriau, M. Hind, A.E. del Río Hernández, M. Griffiths, and C.H. Dean. 2020. The Planar Polarity Component VANGL2 Is a Key Regulator of Mechanosignaling. *Front. Cell Dev. Biol.* 8:1–21, doi: 10.3389/fcell.2020.577201.
72. Volckaert, T., T. Yuan, J. Yuan, E. Boateng, S. Hopkins, J.S. Zhang, V.J. Thannickal, R. Fässler, and S.P. De Langhe. 2019. Hippo signaling promotes lung epithelial lineage commitment by curbing Fgf10 and β-catenin signaling. *Dev.* 146, doi: 10.1242/dev.166454.

FIGURE 1

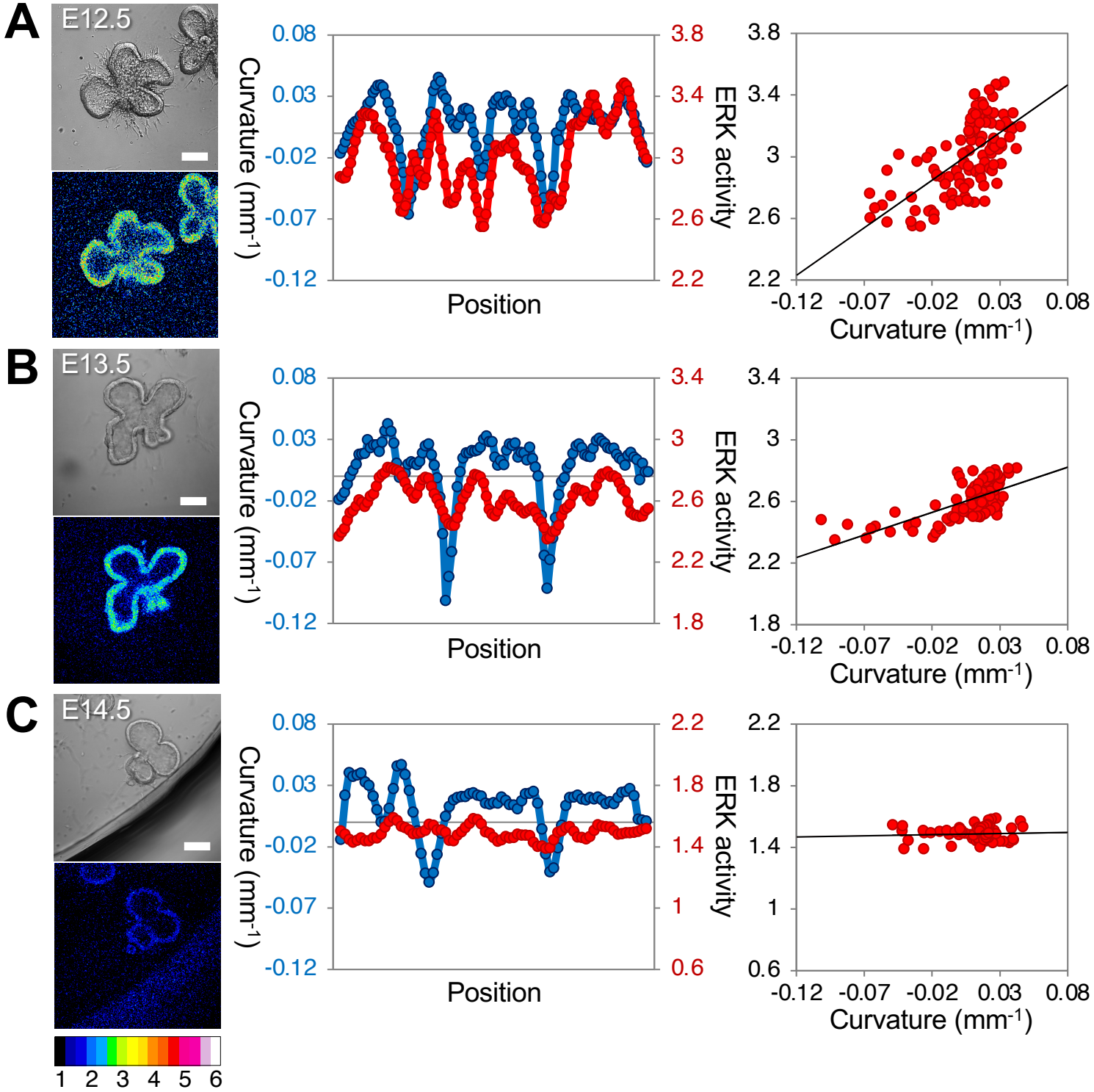
A
E12.5
B
E13.5
C
E14.5
Curvature (mm-1)
ERK activity
Position
Curvature (mm-1)
0.08
0.03
-0.02
-0.07
-0.12
3.8
3.4
3
2.6
2.2
1.8
1.4
1
0.6
1 2 3 4 5 6

FIGURE 2

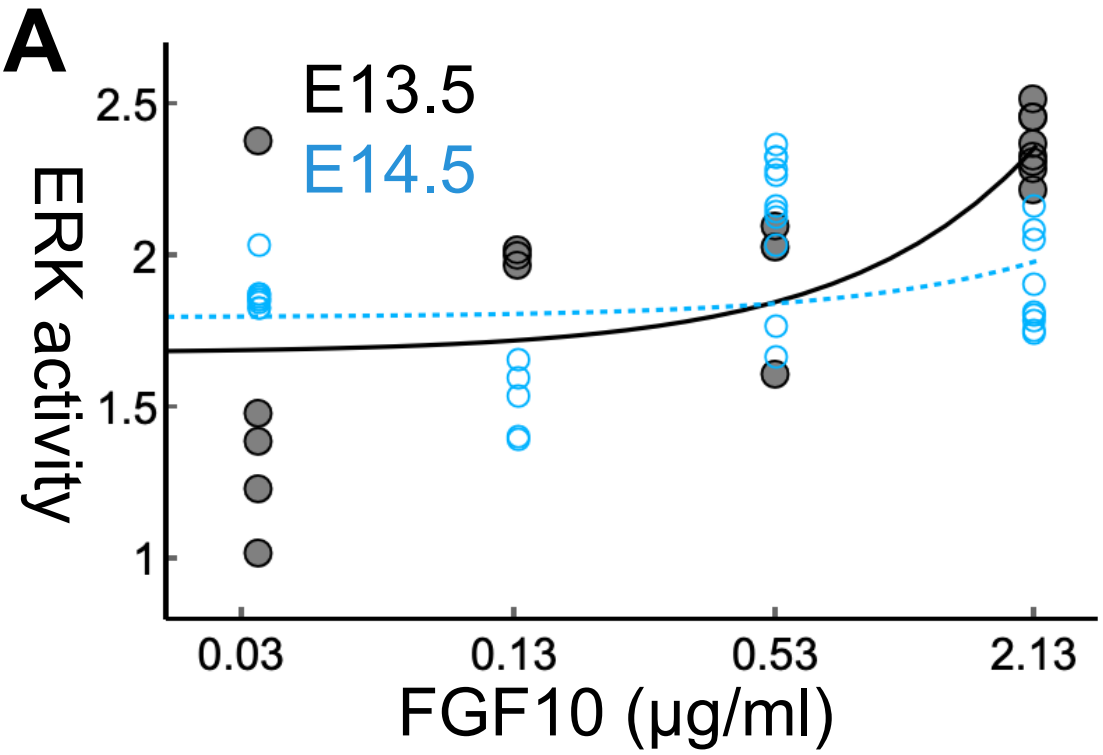
A
E13.5
E14.5
ERK activity
2.5
2
1.5
1
0.03
0.13
0.53
2.13
FGF10 (µg/ml)

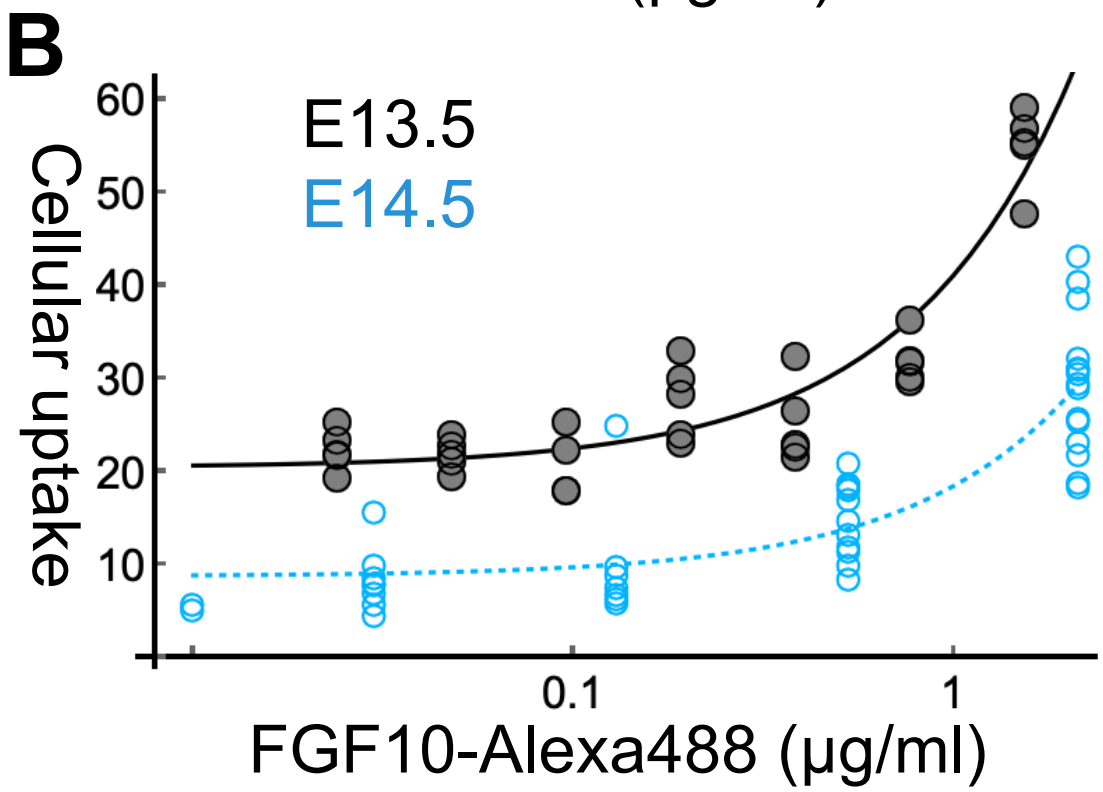
B
E13.5
E14.5
Cellular uptake
60
50
40
30
20
10
0.1
1
FGF10-Alexa488 (µg/ml)

FIGURE 3

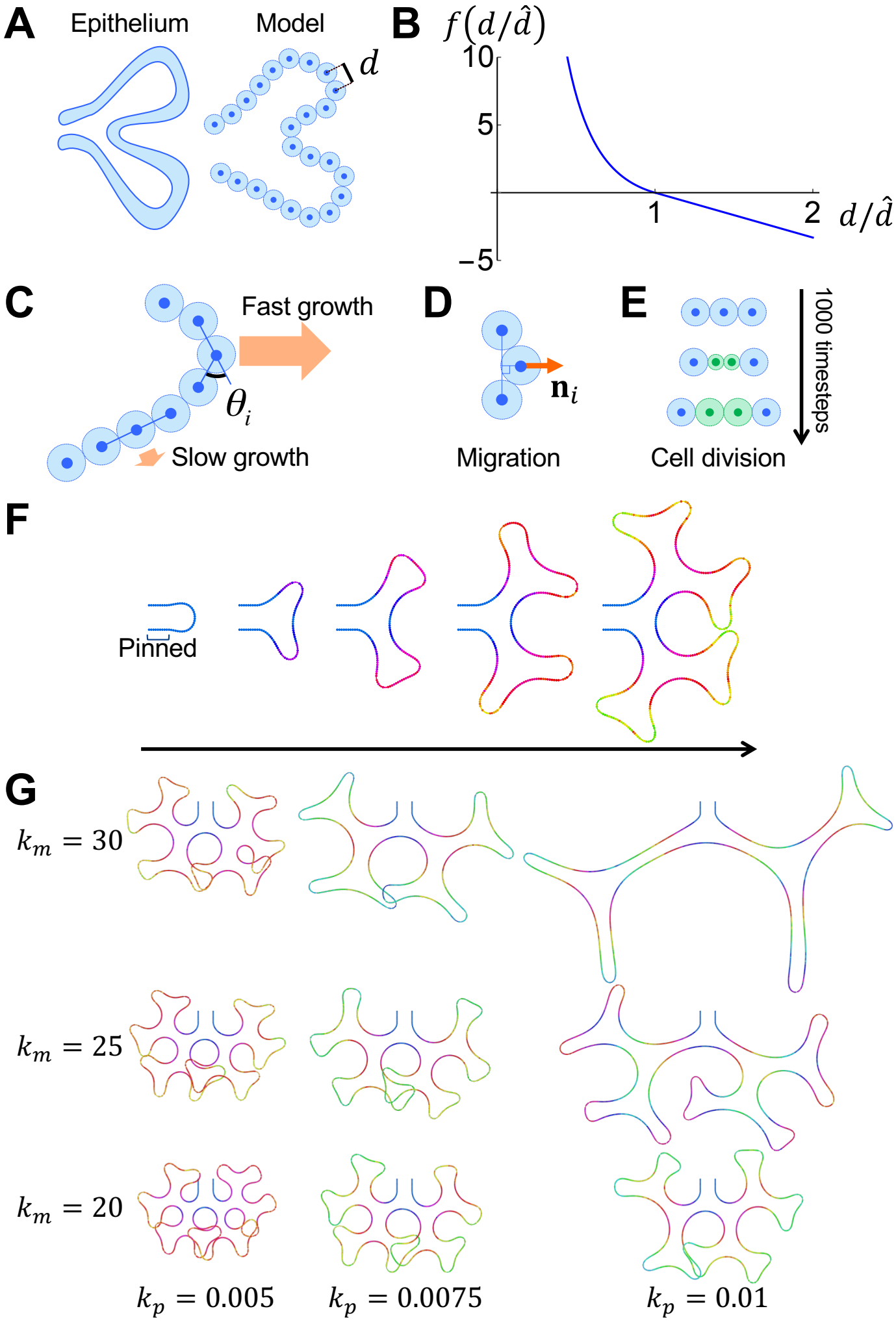
A
Epithelium
Model
d
B
$f(d/\hat{d})$
10
5
−5
1
2
$d/\hat{d}$
C
Fast growth
θ_i
Slow growth
D
$\mathbf{n}_i$
Migration
E
1000 timesteps
Cell division
F
Pinned
G
$k_m = 30$
$k_m = 25$
$k_m = 20$
$k_p = 0.005$
$k_p = 0.0075$
$k_p = 0.01$

FIGURE 4

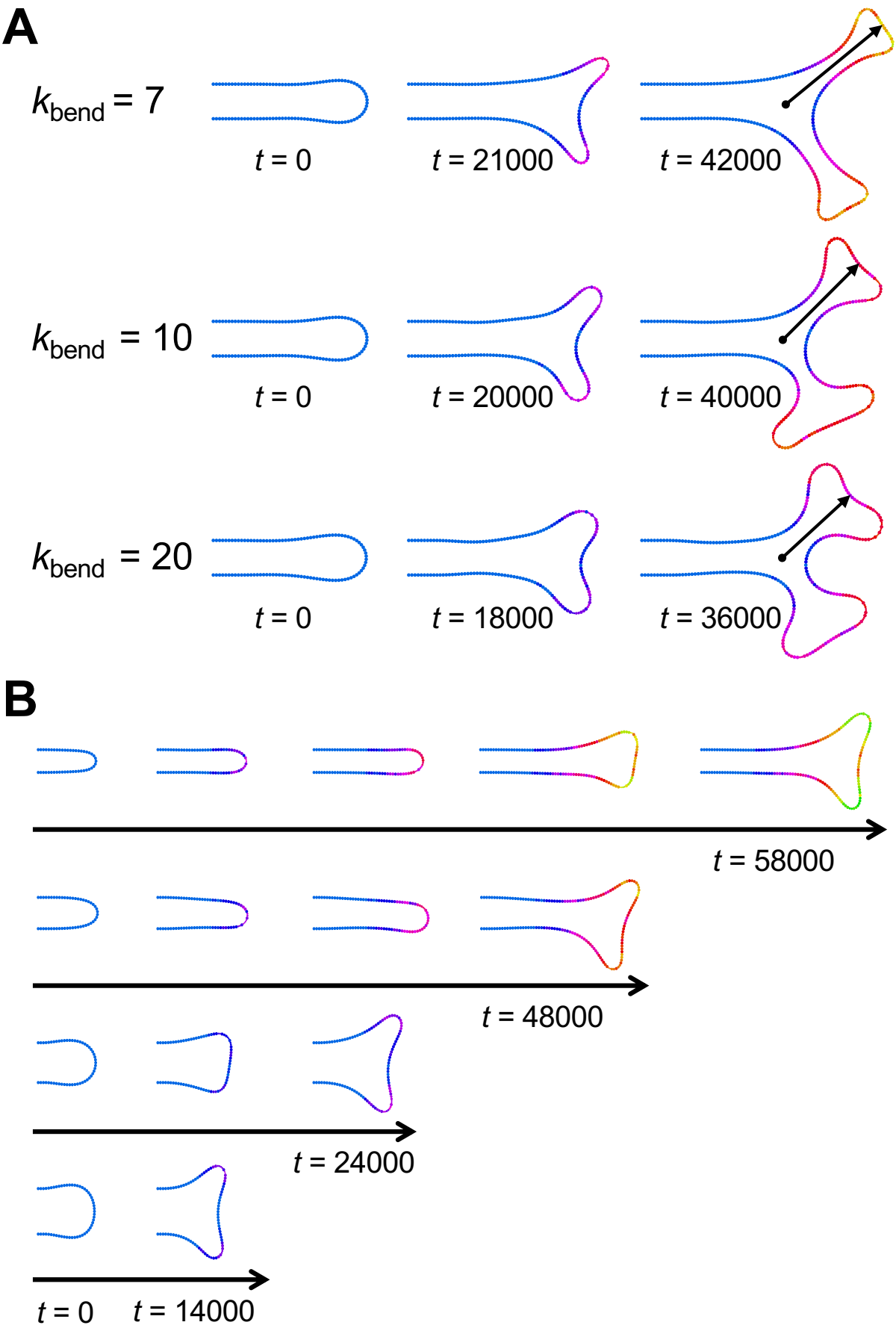
A
k_{bend} = 7
t = 0
t = 21000
t = 42000
k_{bend} = 10
t = 0
t = 20000
t = 40000
k_{bend} = 20
t = 0
t = 18000
t = 36000
B
t = 58000
t = 48000
t = 24000
t = 0
t = 14000

FIGURE 5

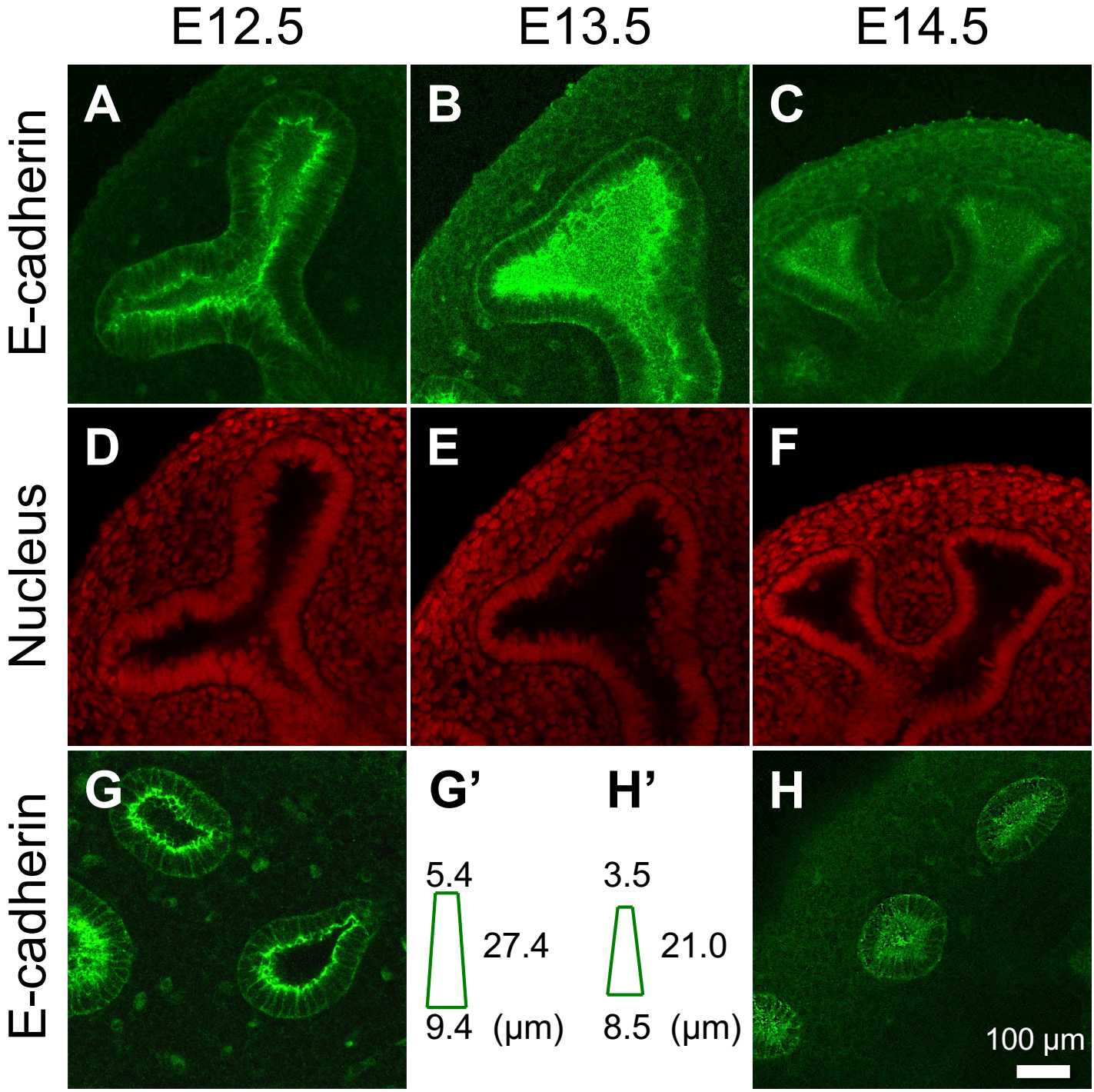
E12.5
E13.5
E14.5
E-cadherin
Nucleus
E-cadherin
A
B
C
D
E
F
G
G'
H'
H
5.4
27.4
9.4 (μm)
3.5
21.0
8.5 (μm)
100 μm

FIGURE 6

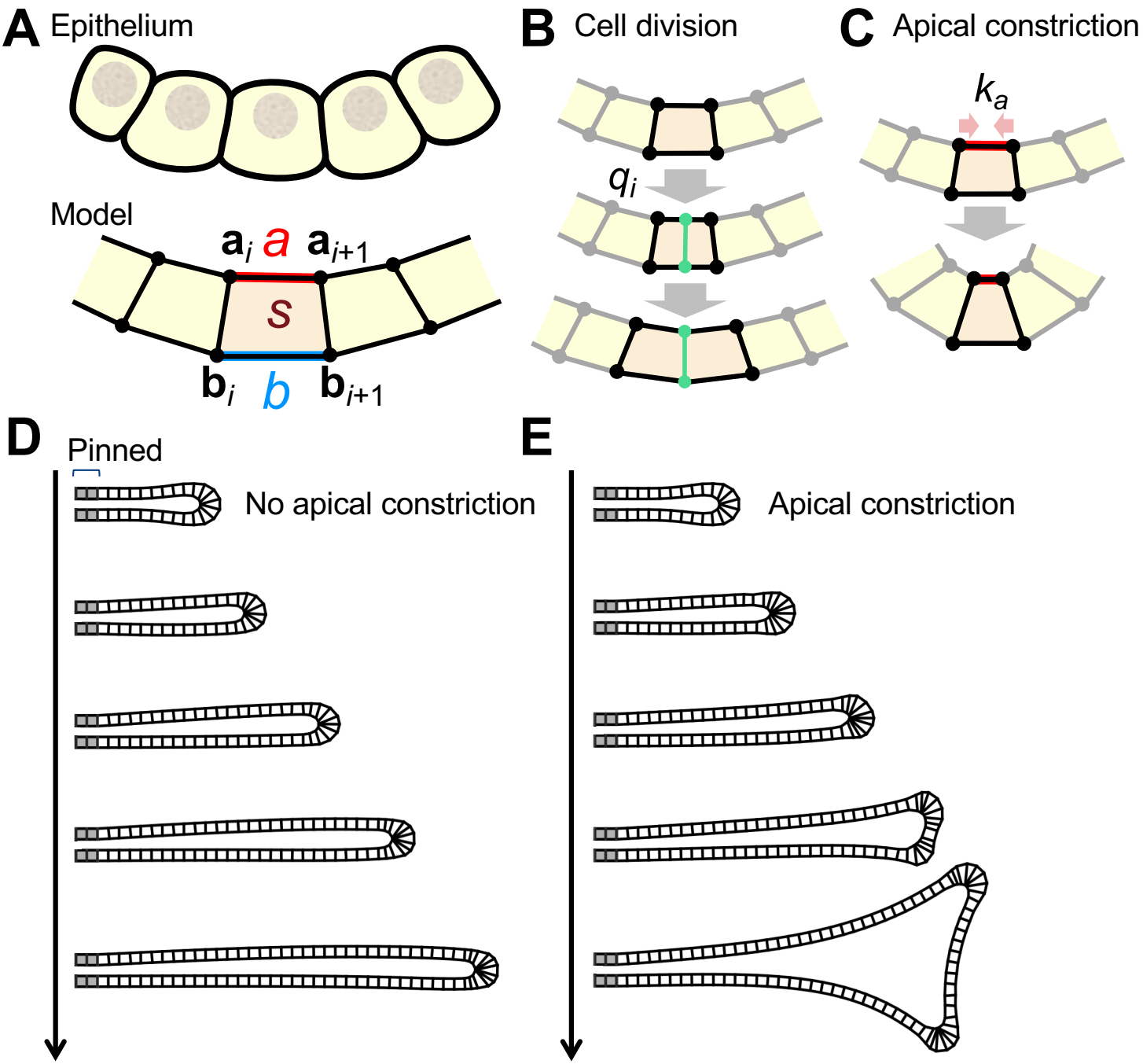
A
Epithelium
Model
$\mathbf{a}_i$ a $\mathbf{a}_{i+1}$
s
$\mathbf{b}_i$ b $\mathbf{b}_{i+1}$
B
Cell division
q_i
C
Apical constriction
k_a
D
Pinned
No apical constriction
E
Apical constriction

FIGURE 7

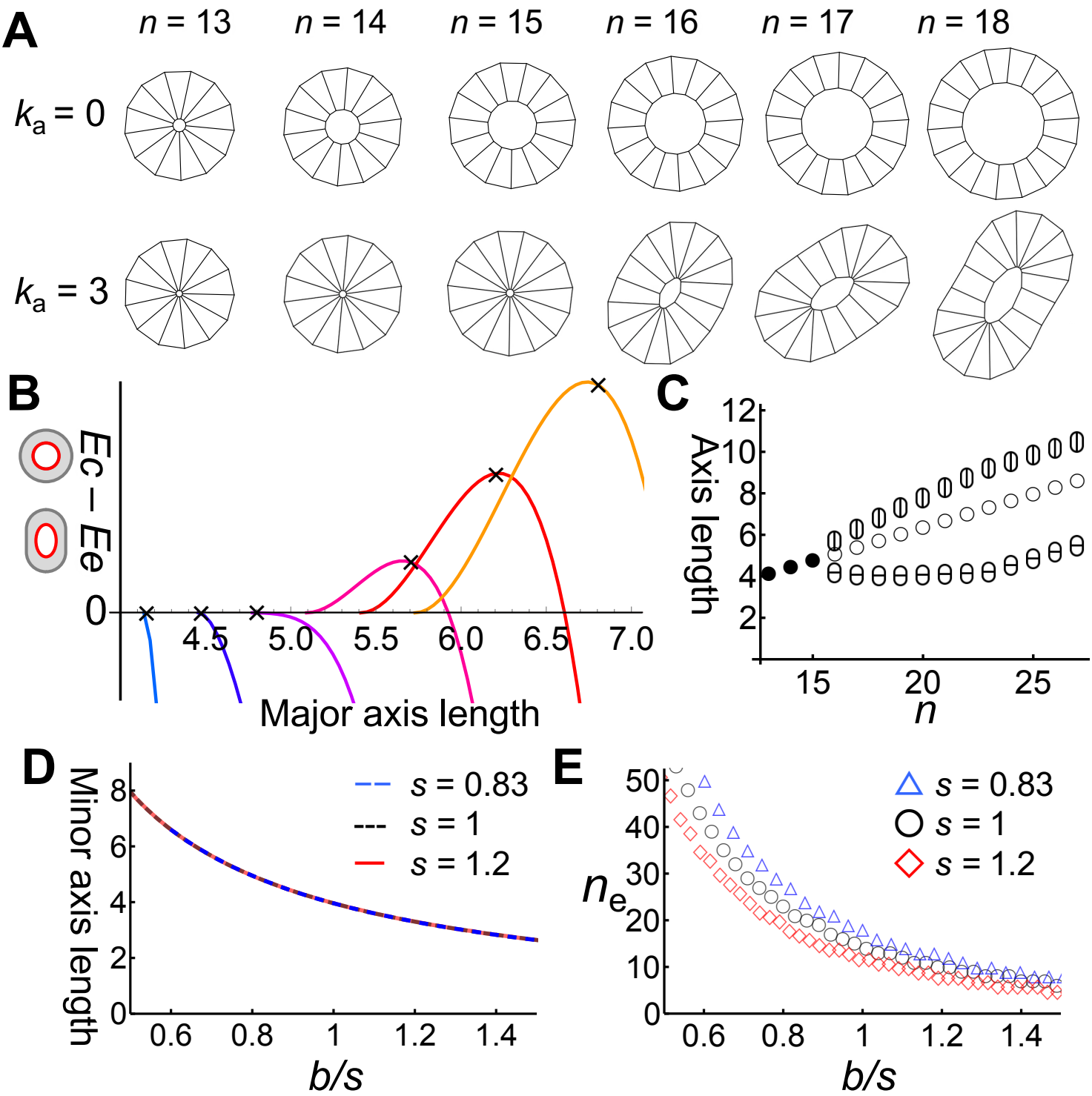
A
n = 13
n = 14
n = 15
n = 16
n = 17
n = 18
ka = 0
ka = 3
B
Ec – Ee
0
4.5
5.0
5.5
6.0
6.5
7.0
Major axis length
C
Axis length
12
10
8
6
4
2
15
20
25
n
D
Minor axis length
8
6
4
2
0
0.6
0.8
1
1.2
1.4
b/s
s = 0.83
s = 1
s = 1.2
E
ne
50
40
30
20
10
0
0.6
0.8
1
1.2
1.4
b/s
s = 0.83
s = 1
s = 1.2

FIGURE 8

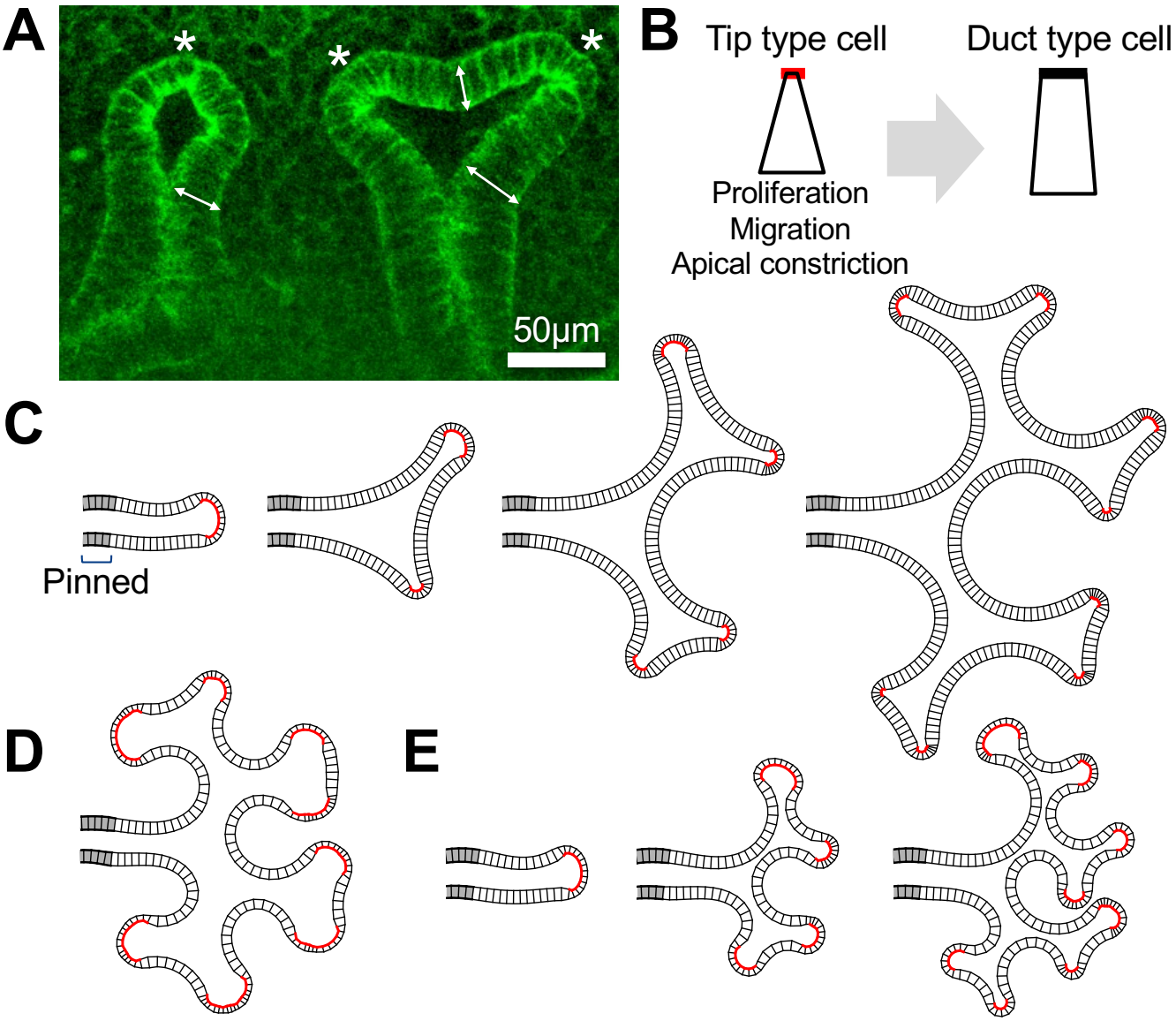

F

	Early phase	Late phase
Response gain lengthens the branch	High	Low
Cell height affects the length and width	High	Low
Apical constriction shapes the tip	Predicted low	Predicted high

Figure Legends

Figure 1

Map of ERK activity in embryonic mouse lungs. The upper left panel is the bright-field image, and the lower left panel shows the heat map representation of ERK activity. The middle panel shows cross-sectional tissue curvature (blue, left axis) and ERK activity (red, right axis) along the epithelial section. The right panel shows the correlation between the curvature and ERK activity. Color bar indicates the range of ERK activity. Epithelium explants at E12.5 **(A)**, E13.5 **(B)**, and E14.5 **(C)** cultured with 500 ng/mL FGF10 for 18 h. Scale bars: 100 μm.

Figure 2

FGF10 dose dependency of the cellular response in E13.5 (black) and E14.5 (blue) epithelium. (**A**) The ERK activity of each cyst is represented by a dot in the semilog plot. The lung epithelium cysts of E13.5 and E14.5 (19 and 34 cysts, respectively) were cultured with FGF10 at the concentration of 0.03, 0.13, 0.53, and 2.13 μg/mL for 18 h. Linear regression analysis showed $y = 0.33x + 1.68$ with $R^2 = 0.53$ for E13.5 and $y = 0.033x + 1.89$ with $R^2 = 0.012$ for E14.5. (**B**) The cellular uptake of FGF10-Alexa488 for 3 h was estimated for 34 and 44 explants of E13.5 and E14.5 lung, respectively. Each dot in semilog plot represents a mean fluorescent intensity in an epithelial area of a cross-section. The concentration of FGF10-Alexa488 was 0.024, 0.048, 0.097, 0.19, 0.38, 0.78, and 1.55 for E13.5, and 0.03, 0.13, 0.53, and 2.13 μg/mL for E14.5. Linear regression analysis showed $y = 20.7x + 20.4$ with $R^2 = 0.87$ for

E13.5, and $y = 9.75x + 8.80$ with $R^2 = 0.72$ for E14.5.

Figure 3

Protrusion growth described by the particle cell model. **(A)** The epithelial cell was represented by the particle in the model. The cell-cell distance is denoted by d. **(B)** The interaction force f in Eq. 2. The parameter $\hat{d}$ denotes the optimal distance between cells. The interaction is repulsive if the relative cell-cell distance $d/\hat{d} < 1$ and attractive if $d/\hat{d} < 1$. **(C)** Protrusion growth was implemented by assuming that migration and cell division occur depending on the angle formed by three consecutive particles. **(D)** Migration occurs in the direction normal to the tissue. **(E)** Cell division was described by replacing a particle to two small particles, which gradually grow to the prescribed size. **(F)** The process of higher-order branching. Snapshots at t = 0, 15000, 30000, 45000, and 60000 are shown. The proximal end with the width 5 was pinned and the distal tip was growing. Particle color indicates the cell generation so that daughter cells were colored differently than the mother cell. The number of cells increased from 50 to 450. $k_{\mathrm{bend}} = 15$, $k_{\mathrm{m}} = 25$, and $k_{\mathrm{p}} = 0.0075$. **(G)** Effect of the curvature dependence on the branch scale. Numerical calculations were done until the number of cells reached 800.

Figure 4

Relation between the branch width and length. (**A**) Bending rigidity broadened the branch tip and shortened the segment length. The initial shape is with the width 5, and $k_{\mathrm{m}} = 20$ and $k_{\mathrm{p}} = 0.0075$ were set. Numerical calculations were done until the

minimum angle at secondary branched regions get lower than -0.02. The segment lengths between the first and second branching points, indicated by arrows, are 17.6 ($k_{\mathrm{bend}} = 7$), 15.2 ($k_{\mathrm{bend}} = 19$), and 13.0 ($k_{\mathrm{bend}} = 20$). **(B)** Branch width extends the segment length. Series of snapshots for cases with the width 4, 5, 6, and 7 are arranged from top to bottom. $k_{\mathrm{bend}} = 15$, $k_{\mathrm{m}} = 30$, and $k_{\mathrm{p}} = 0.01$. Numerical calculations were done until the minimum angle at branched regions get lower than -0.02.

Figure 5

Changes in the epithelial thickness during lung development. **(A–F)** Longitudinal sections of the tips of growing epithelial ducts. E-cadherin immunostaining (A–C) and nuclear staining with PI (D–F) are shown. **(G and H)** Cross sections of the tips. **(G' and H')** The representative cell shape in (G) and (H). The averages of the apical length, basal length, and the cell height are shown. All images are presented on the same scale. Scale bar: 100 μm.

Figure 6

Apical constriction-induced branch formation by the quadrilateral cell model. **(A)** The cross section of epithelium is described as a sequence of quadrilaterals in the model. The *i*-th cell was defined by four vertices the position of which are denoted by $\mathbf{a}_i$, $\mathbf{a}_{i+1}$, $\mathbf{b}_i$, and $\mathbf{b}_{i+1}$. The apical length, basal length, and the cell area are regulated to approach their target values *a*, *b*, and *s*, respectively. Cell migration was described by adding an outward normal vector to $\mathbf{b}_i$. **(B)** Cell division was described by inserting new vertices

to the middle of the edges of a fully grown cell at a probability q_i. The daughter cells are initially set at half the size of the mother cells and grew gradually. **(C)** Apical constriction is described by the attraction between a pair of apical vertices of a cell. The magnitude is represented by k_a. **(D and E)** Comparison of the protrusion growth without and with apical constriction. Snapshots at timesteps $t = 0, 1.5 \times 10^5, 3.5 \times 10^5, 5.5 \times 10^5$, and 7.5×10^5 are shown. Regions of pinned vertices are indicated in red. $k_\mathrm{a} = 0$ (D) and $k_\mathrm{a} = 1$ (E).

Figure 7

Mechanical instability of small cysts by apical constriction in the quadrilateral cell model. **(A)** Cyst of *n* cells was relaxed with $k_\mathrm{a} = 0$ for a sufficient time (upper panels), then apical constriction was introduced by setting $k_\mathrm{a} = 3$ and deformation was observed (lower panels). Parameter values $b = 1$ and $s = 1$ (A–C). **(B)** Subtraction between the estimated potential energies of the circular state *Ec* and the elongated state *Ee*. Different color indicates the different size of the cyst corresponding to (A). Vertical axis indicates the major axis length L, and the minimum corresponds to the diameter in the circular state. Crosses indicate the major axis lengths under $k_\mathrm{a} = 3$ in the model simulations in (A). **(C)** Estimated stable geometry of cysts obtained from potential energy calculations plotted along the cell number n. When $n \leq 15$, the stable shape was circular (closed circle). When $n \geq 16$, the cyst was elongated, and the major axis (ellipse with a longitudinal line) and the minor axis (ellipse with a vertical line) were plotted. The diameter of the circular cyst for $n \geq 16$ was plotted for reference (open circle). **(D)**

Estimated length of the minimum minor axis for any cell numbers. Vertical axis indicates the ratio of the basal length b to the cell area s, set at $s = 1.2$ (blue dashed line), $s = 1$ (black dotted line), and $s = 0.8$ (red line). **(E)** Estimated critical cell number n_e for the shape transition. The minimum number of cells at which the elongated state becomes more stable than the circular state was plotted along b/s.

Figure 8

Integrated model of the protrusion growth and the cell type switching. **(A)** E-cadherin staining of E14.5 mouse lung. Arrows indicate tall cells at concave regions and asterisks indicate short cells at the epithelial tips. **(B)** Concept of the cell type switching. Cells at the high curvature region is assumed to be the tip type, which proliferate, migrate outward, and exert apical constriction. Cells at the low curvature region switches to the duct type, which are tall and do not have those activities. **(C)** Branching process in the case of tall cells with high response gain. Snapshots at $t = 0, 1 \times 10^5, 2 \times 10^5$, and 3×10^5 are shown. Gray cells were pinned at their initial positions, and cells apically marked in red are the tip type. $\varphi_\mathrm{d} = -0.45$, $\rho = 0.00025$, $k_\mu = 0.8$, $k_\mathrm{at} = 35$, and $b = a_\mathrm{d} = 1.1$. **(D)** Branched structure in the case of short cells with the low response gain. $t = 1.4 \times 10^5$, $\varphi_\mathrm{d} = -0.3$, $\rho = 0.0002$, $k_\mathrm{m} = 0.6$, $k_\mathrm{at} = 35$, and $b = a_\mathrm{d} = 1.4$. **(E)** Branching process in the case of short cells with the low response gain and intense apical constriction. Snapshots at $t = 0, 0.7 \times 10^5$, and 1.4×10^5 are shown. $\varphi_\mathrm{d} = -0.3$, $\rho = 0.0002$, $k_\mu = 0.6$. $k_\mathrm{at} = 70$, and $b = a_\mathrm{d} = 1.4$. **(F)** Summary of the predicted regulatory mechanism of lung branch scale. The response gain and cell height were

experimentally observed to be changed during lung development. The model simulation showed that epithelial property affects the branch scale. The model also indicated that apical constriction at the branch tip is effective for changing the branch scale.